

2

3 **Aircraft observations of the lake–land breeze**  
4 **circulation over Lake Victoria ~~from the HyVic pilot~~**  
5 **~~flight campaign~~**

6 **Beth J. Woodhams<sup>1</sup> | John H. Marsham<sup>1,2</sup> | Cathryn E.**  
**Birch<sup>1,3</sup> | Caroline L. Bain<sup>3</sup> | Paul Barrett<sup>3</sup> | Jennifer**  
**K. Fletcher<sup>1,2</sup> | Andrew J. Hartley<sup>3</sup> | Stuart Webster<sup>3</sup>**

The lake–land breeze circulation over Lake Victoria was observed in unprecedented detail with a research aircraft during the HyVic pilot flight campaign. An evening and morning flight observed the lake and land breezes under mostly dry conditions respectively. The lake–land breeze circulation was observed at various heights along a transect and dropsonde and aircraft profiles were taken over the lake and land. Convection-permitting MetUM simulations with a variety of horizontal grid-spacings were run for the flight period. During the evening flight, the aircraft crossed the lake breeze front over land at 1627 LT, approximately 50 km to the east of the lake shore, recording a decrease in specific humidity of  $6 \text{ g kg}^{-1}$  and a reversal in wind direction over a horizontal extent of  $\sim 5 \text{ km}$ . The sharp gradient in wind and moisture were captured by the simulations with 1.5 km and 300 m horizontal grid-spacing, but the 4.4 km simulation was unable to capture the sharpness of the transition out of the lake breeze air. At least one region of elevated moisture (previously seen in simulations but never observed), coincident with cloud and increased turbulence, was observed over the lake surface during the early morning. However, the mechanism for the formation of the elevated moisture was unclear. The lake breeze and moist layer over the lake during the evening and morning flights respectively were too deep in the model. The lake breeze was also drier in the model than observed, suggesting a dilution of the lake breeze air. These model issues are likely linked to deficiencies in the representation of lake and land surface temperatures, as well as in sub-grid mixing. Overall, this pilot campaign provides an unprecedented snapshot of the Lake Victoria lake–land breeze circulation and motivates a more comprehensive field campaign in the future.

**Keywords** — Lake Victoria, East Africa, lake–land breeze circulation, observations, research aircraft

<sup>1</sup>Institute for Climate and Atmospheric Science, School of Earth and Environment, University of Leeds, Leeds, LS2 9JT, United Kingdom

<sup>2</sup>National Centre for Atmospheric Science, University of Leeds, Leeds, United Kingdom

<sup>3</sup>Met Office, Exeter, United Kingdom

#### Correspondence

Beth J. Woodhams, Institute for Climate and Atmospheric Science, School of Earth and Environment, University of Leeds, Leeds, LS2 9JT, United Kingdom

Email: B.J.Woodhams@leeds.ac.uk

#### Funding information

Funder One, Funder One Department, Grant/Award Number: 123456, 123457 and 123458; Funder Two, Funder Two Department, Grant/Award Number: 123459

## 1 | INTRODUCTION

Storms and high winds over Lake Victoria are estimated to contribute to 5,000 fatalities on the lake every year (Cannon et al., 2014). An estimated 3.5 million people rely on the lake for their livelihoods, including 200,000 fishers (Semazzi, 2011). The



lake also supports transport and trade routes, as well as hydroelectric power. However, forecasting severe weather in East Africa remains a great challenge for NWP (Numerical Weather Prediction) models, despite the introduction of a convection-permitting (CP) forecast model over East Africa by the UK Met Office (Chamberlain et al., 2014; Woodhams et al., 2018). Although explicit convection does show an improvement in the diurnal cycle of rainfall and representation of convective storms compared to forecasts from the global operational system, biases in rainfall timing and amount persist.

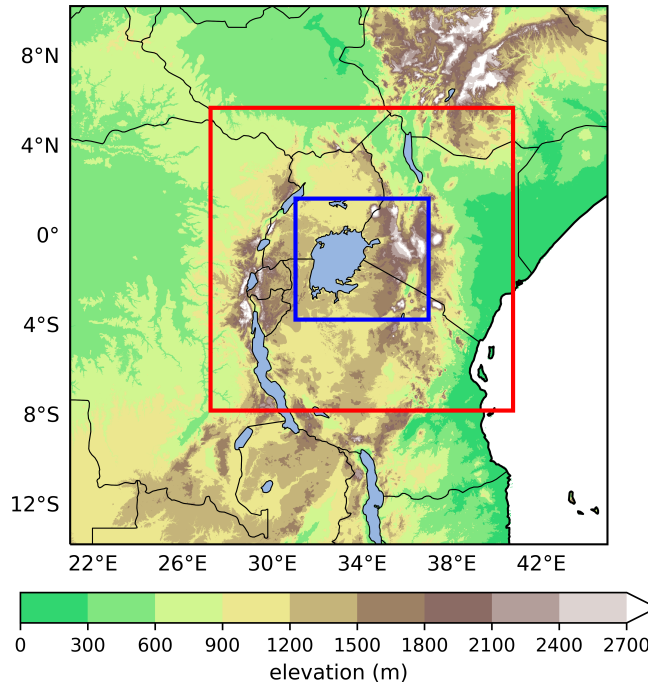


FIGURE 1 Elevation data are from the Global Land One-kilometer Base Elevation (GLOBE) Digital Elevation Model (Hastings and Dunbar, 1999). Full domain, red line and blue line correspond to 4.4 km, 1.5 km and 300 m nests respectively for CP MetUM runs during the HyVic period.

The lake–land breeze circulation has long been understood to play a key role in modulating and enhancing convection over the Lake Victoria basin. Flohn and Fraedrich (1966) noted the existence of a diurnal circulation system, driven by temperature and moisture gradients between the lake and land. Their study linked the early morning maximum of rainfall over the lake to convergence produced by the nocturnal land breeze. Conversely, a divergent lake breeze forms during the day, suppressing convection over the lake, but enhancing convection along the lake breeze front over land (Datta, 1981; Ba and Nicholson, 1998). The lake and land breezes are also reinforced by anabatic and katabatic flows respectively, especially on the steep slopes of the Gregory Ridge to the east (Fig. 1 (Lumb, 1970; Okeyo, 1986; Mukabana and Pielke, 1996; Anyah et al., 2006; Thiery et al., 2015). Thiery et al. (2016) showed a statistical link between intense daytime storms over surrounding land and the occurrence of intense storms over the lake the following night, linked to enhanced low-level convergence and moisture availability as a result of the daytime storms. This correlation was used to create an early warning system for the most intense storms over the lake, with high accuracy but short lead times Thiery et al. (2017). Van de Walle et al. (2020) showed that convergence over the lake

East Africa experiences two rainfall seasons each year—MAM (Long Rains) and OND (short rains)—which coincide with the passage of the tropical rain belt across the region, although the lake basin is fairly wet throughout the year. Prevailing winds

28 have an easterly component throughout most of the troposphere due to the position of the lake on the equator. The majority of  
29 moisture availability is a result of advection of moist air from over the Indian Ocean, although the Kenyan Highlands to the east  
30 of the lake block much of this flow (Mukabana and Pielke, 1996; Anyah et al., 2006). Finney et al. (2020) showed that daily  
31 mean rainfall is greatly enhanced (by up to 100% in some months) on days where flow is westerly across the region, attributed to  
32 the inflow of moisture from the Congo Air Mass. On the other hand, daily mean rainfall was shown to be suppressed in regimes  
33 of strong easterly flow.

34 Previous studies of Lake Victoria have tended to focus on the mean diurnal cycle, thereby neglecting the impact of daily  
35 variability, and smoothing out small-scale details. For the first time, Woodhams et al. (2019) (from hereon W19) investigated  
36 individual case studies of the lake–land breeze circulation and storm events over Lake Victoria, using a CP version of the Met  
37 Office Unified Model (MetUM) with 1.5 km horizontal grid-spacing. In the chosen cases studies, afternoon convergence over  
38 land to the east of the lake (at the lake breeze front) was pushed back over the lake at night as the lake breeze weakened and the  
39 land breeze developed (reinforced by the prevailing easterlies and likely a katabatic component). In other words, the daytime  
40 convergence over land and nocturnal convergence over the lake were caused by a persistent line of convergence which propagated  
41 from land to lake, rather than being two separate features. In a case study taken from the Long Rains season (MAM), this  
42 propagation was shown to be responsible for the lake-ward propagation of a storm which formed to the east of the lake. W19  
43 also noted the overnight formation of a bulge of moisture extending  $\sim 1$  km above the lake surface, formed along the convergence  
44 line as it propagated westward, and reinforced later as a land breeze also formed across the western shore (W19, their Fig. 14). ~~It~~  
45 ~~was suggested~~ that the properties of this moisture bulge (moisture content and depth) could determine whether or not a storm  
46 formed. The lake–land breeze circulation and the results of W19 are described in more detail in section 2.

47 The processes and features described in W19 were based almost entirely on model simulations, ~~given the lack of in-situ~~  
48 ~~observations in the region~~. Existing in-situ observations of the lake–land breeze circulation have been obtained from weather  
49 stations with fixed locations (e.g. Lumb 1970; Datta 1981), with which it is difficult to build a full picture of the circulation. Data  
50 from such stations is generally recorded with a maximum frequency of 15 minutes, too low to fully capture the passage of the  
51 lake or land breeze fronts. In addition, such stations can only sample the circulation at the surface. Upper-air observations are  
52 particularly lacking in the region, and observations over the lake itself present an exceptional challenge. As such, the vertical  
53 structure of the lake–land breeze and moisture bulge have not been observed. An additional challenge is that many weather  
54 stations in the region are owned by private companies or the national meteorological services, and data is not easily accessible to  
55 researchers.

56 For forecasting severe weather over the region, Woodhams et al. (2018) showed that a CP version of the MetUM does  
57 add value to a global (parametrised) model forecast, in particular on sub-daily timescales, although skill remains limited. A  
58 substantial amount of storms over Lake Victoria are not forecast and false alarm rates are also high. Likely reasons for poor  
59 model skill in such configurations (likely over the tropics as a whole) include unresolved trigger mechanisms and a lack of  
60 observations—especially upper air—for data assimilation. A lack of observations also prevents detailed model verification and  
61 subsequent development.

62 In January 2019, the HyVic pilot flight campaign took place, using the Facility for Airborne Atmospheric Measurements  
63 (FAAM) BAe-146 aircraft to observe the lake–land breeze circulation over Lake Victoria. The campaign consisted of an evening  
64 and morning flight, both with a duration of approximately 4 hrs, to sample the lake and land breeze components of the circulation  
65 respectively during a period with very little rainfall and without the presence of a major storm to complicate the flows and  
66 analysis. Although observations of storms would be very beneficial, the aircraft is not able to fly in such conditions. In particular,  
67 these flights aimed to investigate some of the features simulated by the model in W19, such as the moisture bulge; characterise  
68 the lake and land breeze fronts; and collect observations to be used for model verification. In this paper, the two flights will be  
69 introduced and a detailed description of the observations from the lake and land breeze regimes will be presented. High-resolution  
70 CP MetUM simulations were run for the HyVic period. The model simulations are presented as a companion to understand

71 which processes are consistent between observations and model and how resolution impacts this. ~~For this reason a model with~~  
72 ~~300 m horizontal grid spacing is used, which is far higher resolution than any operational model currently in the region.~~

73 This short campaign was designed as an add-on to the MOYA campaign based in Entebbe, Uganda (measuring methane over  
74 tropical Africa, Allen et al. 2019; Barker et al. 2020) and was a pilot for a potential more comprehensive campaign in the future.  
75 Given the high seasonal and sub-seasonal variability in moisture availability and circulation in the region (e.g. Yang et al. 2015;  
76 W19), it is noted that the two flights presented in this paper cannot be used to draw robust conclusions about the lake–land breeze  
77 circulation on all days. However, this novel set of observations can still provide a snapshot of the lake–land breeze circulation in  
78 unprecedented detail, be used for detailed evaluation of model performance, and inform future field campaigns.

79 Section 2 provides a more extensive literature review of the lake–land breeze circulation of Lake Victoria to motivate the  
80 aims of the campaign. 3 introduces the flight tracks, aircraft observations and other observational data. The accompanying model  
81 simulations are also introduced. In section 4.1 the general meteorological conditions during the campaign are described. Sections  
82 4.2 and 4.3 present and discuss the observations from the evening and morning flights respectively. Conclusions drawn in section  
83 5.

## 84 2 | BACKGROUND

85 This section provides an overview of the current understanding of the lake–land breeze circulation in literature. In particular,  
86 insights from the high-resolution simulations in Woodhams et al. (2019) are used to set out aims for the flight campaign. W19  
87 presented simulations of a dry period in July, a large storm during May (Long Rains season) and a smaller storm from July (dry  
88 season), of which the dry period simulation is most relevant for flight planning.

89 During the late afternoon, lake breezes form over the shorelines of Lake Victoria as density gradients between the warmer,  
90 drier air over land and cooler, moister air over the lake drive density current-like flows of air from the lake toward the land. The  
91 lake breeze front marks the leading edge of the advected lake air and is a region of low-level convergence and strong gradients  
92 in moisture and temperature. Convergence is generally strongest to the east of the lake where the lake breeze runs into the  
93 prevailing easterly winds. In the dry period case study in W19, the lake breeze across the eastern shore occurred over a depth of  
94 ~1 km (their Figs. 7c,i,o). The lake breeze front reached its maximum extent inland (80 km) at 1800 LT and was associated  
95 with enhanced upward motion and the transport of moist air aloft. Uplift and moist air at the lake breeze front favour convective  
96 initiation in this region (e.g. Datta 1981; Ba and Nicholson 1998; Thiery et al. 2015; W19). Simulations in both Thiery et al.  
97 (2015) and W19 showed the occurrence of a return flow between ~2–5 km MSL (~1–4 km AGL), which advects the moist air  
98 back toward the lake and induces subsidence over the lake surface. A return flow also occurs to the east of the lake breeze front  
99 (manifested in a reduction in the prevailing southeasterlies in the mid-levels), resulting in divergent flow above the lake breeze  
100 front. Based on W19 and the other studies, the HyVic evening flight was designed to sample the lake breeze front and return flow,  
101 both of which are difficult to observe using ground-based weather stations with fixed positions and low measuring frequency.

102 In W19 dry period simulation, the afternoon convergence along the lake breeze front to the east of the lake propagated  
103 westward over the lake between ~2200–0900 LT (their Figs. 7d-f,j-l,n-r and Fig. 14). This propagation back over the lake was  
104 attributed to the formation of a land breeze in the lowest few hundred metres across the eastern shore around 2200 LT. The lake  
105 breeze was later encompassed by a strengthened prevailing easterly flow over a depth of ~2 km around 0200 LT. This easterly  
106 flow was shown to push the convergence across the lake toward the western shore. In the W19 simulation, the density current-like  
107 flow (identified by low virtual potential temperature,  $\theta_v$ ) from the land collided with the stable air over the lake, causing the  
108 moist near-surface air to be lofted upward into a shallow bulge with a depth of a few hundred metres that propagated westward  
109 with the convergence (W19, their Fig. 7d-e,j-k). A shallow land breeze also formed across the western (opposite) shore around  
110 0200 LT, which reinforced the convergence. The centre of the moisture bulge was located over the centre of the lake at 0200 LT

111 and over the western shore at 0900 LT (W19, their Figs. 7k and 7l respectively). This bulge feature has not previously been  
 112 observed, therefore its existence is hypothesised based only on the W19 simulation. The main aim of the HyVic morning flight  
 113 was to locate and observe this feature (if possible) to understand more about its properties.

### 114 3 | METHODS

#### 115 3.1 | Flights

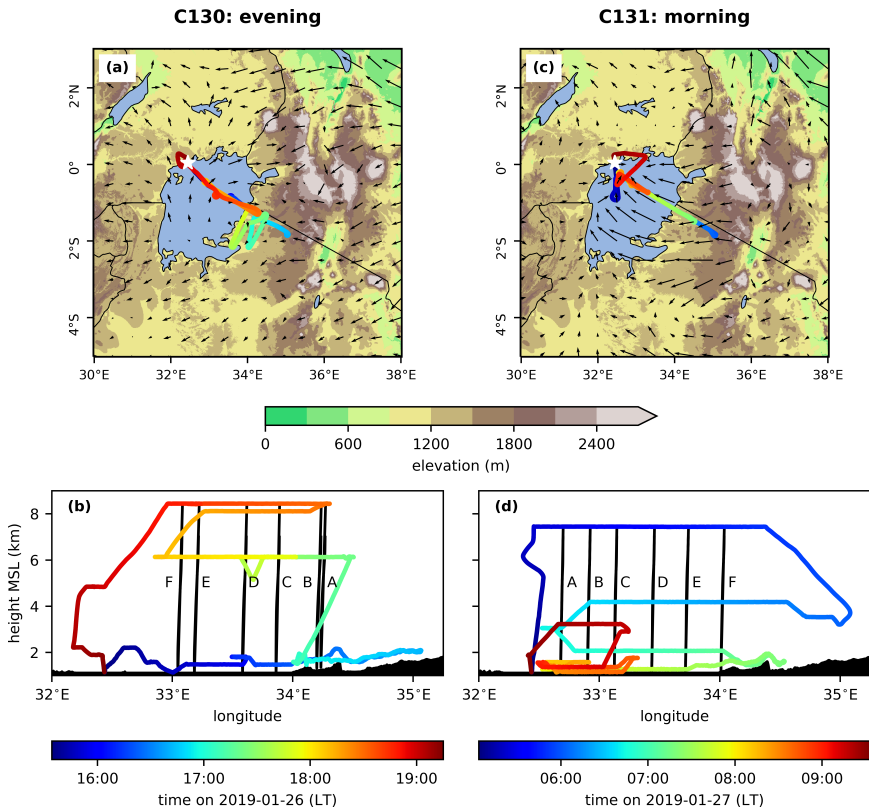


FIGURE 2 (a)(c) Map view of flight track showing terrain height (shading) and mean 10 m wind vectors from ERA5 (Hersbach et al., 2020) during the flight duration and (b)(d) cross-section view of the flight track for (a) C130 (evening) C131 (morning). Colours along the flight track show the time of day. White star in (a,c) marks Entebbe airport. Black lines in (b,d) show the dropsonde paths.

#### 116 3.1.1 | Flight planning

117 This study was performed using the FAAM BAe-146 aircraft, operating out of Entebbe (white star, Figs. 2a,c). The campaign  
 118 consisted of two flights: one in the evening to observe the lake breeze, and one the following morning to observe the  
 119 land breeze. Given the lack of previous observational data, much of the flight planning was based on the dry period simulation in W19, and

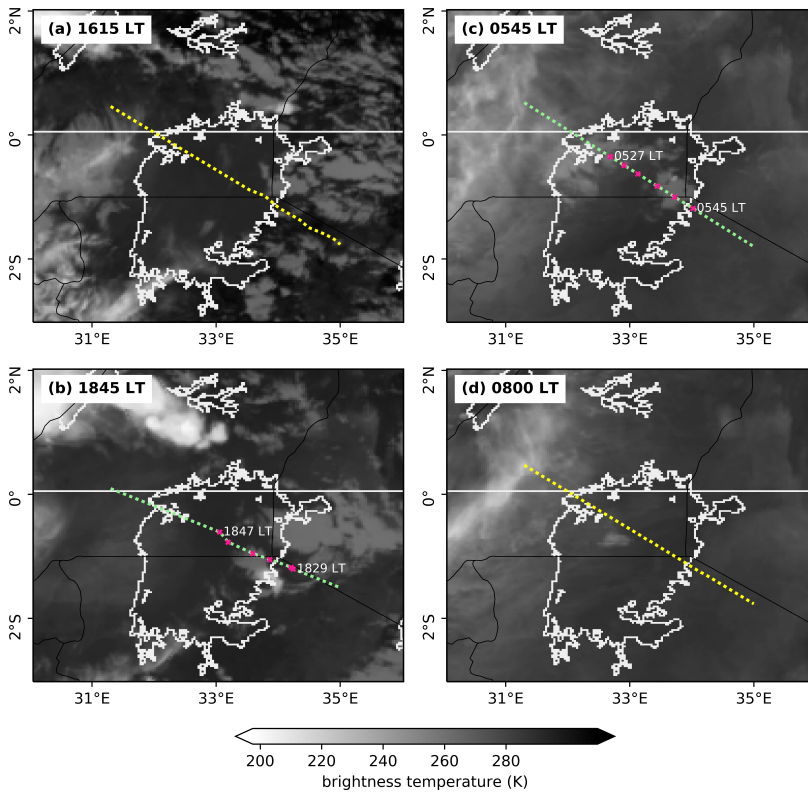


FIGURE 3 METEOSAT 10.8  $\mu\text{m}$  brightness temperature images closest to the times of the sonde drops/runs. Yellow and green dashed lines mark transect along which model cross-sections are computed for flight runs and sonde transects respectively. Pink crosses show where the sondes were dropped, with the time of the first and last drop labelled.

120 ~~overview of which was given in~~ [Figure 2](#). Given that the W19 case study was taken from July, forecast data from the 4.4 km Met  
 121 Office operational Tropical Africa model (Hanley et al., in review) for January and February 2018 were also used to inform the  
 122 flight plans (section 4.1 provides a description of the synoptic differences between these months). However, the operational data  
 123 was on a coarser grid and had reduced model output times and variables compared to the simulations in W19.

124 ~~In particular,~~ it was important that the morning flight directly followed the evening flight; W19 showed that onshore  
 125 convergence to the east of the lake during the evening propagates across the lake overnight, therefore the same ‘system’ could  
 126 be sampled in both flights. The flights were timed to sample the mature lake and land breezes, whilst also taking into account  
 127 constraints on aircraft and crew turnaround between flights and the minimum safe altitude when flying in the dark. For safety  
 128 reasons, flights could only take place when there were no significant storms. Flight times are summarised in Table 1.

129 Both flights were based along an approximately northwest to southeast transect between Entebbe (on the northwest shore  
 130 of the lake) and approximately 130 km onshore from the eastern shore in Tanzania (Fig. 2). This transect was flown at several  
 131 altitudes in order to observe the lake and land breezes in two dimensions. During both flights, six sondes were dropped from the  
 132 highest leg of the transect to obtain full profiles throughout the lower troposphere. The aircraft transect was chosen to be similar  
 133 to the model transect analysed in W19, whilst also choosing a navigable path over terrain to the east of the lake. Lake Victoria  
 134 itself sits at 1,135 m above mean sea level (MSL).

Flight	Date	Takeoff	Landing	Entebbe sunset or sunrise
C130	26 Jan 2019	1234 UTC/ 1534 LT	1615 UTC/ 1915 LT	1606 UTC/ 1906 LT
C131	27 Jan 2019	0208 UTC/ 0508 LT	0637 UTC/ 0937 LT	0359 UTC/ 0659 LT

TABLE 1 A summary of the flights performed as part of the HyVic pilot field campaign.

### 3.1.2 | C130: Evening flight

A map view and along-transect vertical cross-section view of the evening flight are shown in Figs. 2a and b, respectively. The flight began with a terrain-following leg at ~300 m above ground level (AGL) (~1450 m MSL over the lake, blue colours) which passed from the lake onto the land, to sample the lake breeze near to the surface. This leg was briefly interrupted over the lake whilst awaiting air traffic control clearance. The low-level leg was followed by a return leg at ~6000 m MSL (yellow colours) to sample the mid-level return flow. Between these along-transect legs, two legs were flown approximately perpendicular to the transect (parallel to the lake breeze front, green colours) at the lower and upper altitudes, but these are not included in the analysis. The aircraft then ascended to ~8500 m MSL and dropped six sondes from east to west, including two over land and four over the lake (Fig. 2b, orange-red colours and Fig. 3b, pink crosses). This flight pattern enabled low-level flying to take place in daylight with the dropsondes at dusk.

### 3.1.3 | C131: Morning flight

The morning flight track is shown in Figs. 2c,d. This flight began with the highest leg (~7500 m MSL, dark blue colours), along which six sondes were dropped from west to east, the first five over the lake and the final sonde just on the shoreline (Fig. 2d and Fig. 3c, pink crosses). In this case, the highest leg was completed first given altitude restrictions in the dark. The aircraft then performed two further legs at ~4000 m (light blue colours) and ~2000 m MSL (teal colours). As the latter leg reached the shoreline, the aircraft descended to ~300 m AGL (~1450 m MSL over the lake), until turning 180° ~75 km inland and continuing back toward the lake, following the terrain at this height (green-yellow colours). Once over the lake, the aircraft descended to 150 m AGL (~1300 m MSL) to complete the return leg. From the sonde drops, an approximate location of a moisture bulge was identified and this was then sampled at various heights between 30 and 500 m AGL (1165–1635 m MSL, yellow-red colours) and with two aircraft profiles. Aircraft profiles were also performed over the centre of the lake (orange colours), to compare profiles inside and outside the bulge region. Based on W19, the ideal time to search for the bulge feature and sample over-lake convergence would have been around 0200 LT, but restrictions on low-level flying in the dark meant that the near-surface could not have been sampled at this time. As a result, the sondes were dropped before sunrise, allowing low-level flying to begin at first light.

## 3.2 | Aircraft data

Data were collected using in situ instrumentation carried by the BAe-146 aircraft, described in some detail by Mirza (2016). During science sampling, the aircraft maintains an Indicated Airspeed of 210 knots which, given the altitude of the lake, results in a True Airspeed ~120 ms<sup>-1</sup> when sampling in situ.

Temperature data were collected by a loom-type platinum resistance thermometer which was located in a non-deiced Rosemount Temperature housing. Data were recorded at 32 Hz and reported at 1 Hz which. While measurements are susceptible to drift, this type of instrument is expected to have accuracy better than +/- 0.5K.

Humidity was sampled using a combination of a slow-response well-calibrated chilled-mirror hygrometer (Buck CR2) and a fast response tunable-diode laser hygrometer Water Vapour Sensing System-II (WVSS-II). While the WVSS-II is not calibrated, chilled-mirror hygrometers are known to suffer from excursions when sharp humidity gradients are crossed. Therefore, the fast-response WVSS-II instrument was first compared to the Buck in known 'good' periods—away from large humidity gradients and altitude changes—and showed good agreement. This allowed WVSS-II to be used to sample the more challenging environments. Data are reported at 1 Hz. A flush-mounted inlet was used to provide the sample to WVSS-II. The location of the flush-mounted inlet within the aircraft boundary layer is not expected to compromise the measurements as it has been shown to perform as well as a Rosemount inlet when sampling humidity concentrations  $> 1.0 \text{ g m}^{-3}$  (Vance et al., 2015), which is significantly lower than any humidity values encountered during this case study.

Three-dimensional wind components were sampled at 32 Hz using a nose-mounted 5-port turbulence probe (Mirza et al., 2016). Data were combined with position and aircraft altitude information from a GPS-aided Inertial Navigation Unit (GIN) and rotated on to the transect heading to give along-transect wind speeds at 1 Hz. Quality control analysis showed some evidence of a weak heading dependency to wind direction in the data. This is likely related to imperfectly specified calibration coefficients for alignment of GIN components resulting in rotation errors for the wind vector. Comparison of the rotated along-transect wind speeds with a supplementary turbulence probe located on the wing—the AIMMS20 (Beswick et al., 2008)—showed good agreement (not shown) suggesting that this error is not significant for this study. Vertical velocity perturbations at 32 Hz around the mean value are taken as a proxy for turbulence intensity since turbulent kinetic energy (TKE) is proportional to  $w'^2$  (Petersen and Renfrew, 2009).

Temperature, pressure and humidity were also measured using Vaisala RD94 dropsondes launched from the aircraft when at high altitude. Data were transmitted to the Airborne Vertical Atmospheric Profiling System (AVAPS) receiver on board the aircraft at a frequency of 2 Hz. The fall speed of the sonde varied from  $\sim 10\text{--}15 \text{ ms}^{-1}$ , therefore measurements were taken every  $\sim 5\text{--}8 \text{ m}$ .

### 3.3 | MetUM simulations

CP MetUM simulations were run for the campaign period. The regional model setup was the same as that described in W19—based on the Even Newer Dynamics for General atmospheric modelling (ENDGAME) dynamical core (Wood et al., 2014)—except with the new Regional Atmosphere 1 for the Tropics (RA1T, Bush et al. 2019) configuration. Of note is the use of the zero lateral flux (ZLF) scheme of Zerroukat and Shipway (2017), which ensures that mass is conserved and reduces the excessive rainfall rates seen in Woodhams et al. (2018). Simulations were triply one-way nested, with horizontal grid-spacings of 4.4 km, 1.5 km and 300 m (Fig. 1). The 4.4 km nest was driven by boundary conditions from the European Centre for Medium-Range Weather Forecasts (ECMWF) Integrated Forecasting System (IFS) model. The regional model nests had 80 terrain-following vertical levels up to a lid of 38.5 km and were run with timesteps of 150, 60 and 15 s for the 4.4 km, 1.5 km and 300 m nests respectively. Model data was output every 4 hour. Runs initialised at 2019/01/25 0000 UTC and 2019/01/25 1200 UTC were used to compare to aircraft data from the evening and morning flights respectively. \*ADD LAKE SURFACE TEMPS\*

### 3.4 | Satellite observations and analyses

Brightness temperatures were computed from the  $10.8 \mu\text{m}$  IR satellite images produced by the Spinning Enhanced Visible and Infrared Imager (SEVIRI) instrument on board the Meteosat Second Generation Satellite (Schmetz et al., 2002). The digital number in the image was converted to brightness temperature using the relationship in Chamberlain et al. (2014) (their equations 1-2). Rainfall rate observations from the IMERG Final Precipitation version 06 product on a  $0.1^\circ$  grid from the Global Precipitation Measurement (GPM) mission (Huffman et al., 2019b,a) were used to compute rainfall anomalies for the period. A



205 full description and review of GPM can be found in W19. Analyses from ERA5 (Copernicus Climate Change Service (C3S),  
 206 2017; Hersbach et al., 2020) on a 0.25° grid with 37 pressure levels and time resolution of 1 hour are used to compare the study  
 207 period with climatology.

### 208 3.5 | Derived variables

209 Potential temperature  $\theta$  was derived from observations and simulations using:

$$\theta = T \left( \frac{P_0}{P} \right)^{\frac{R_d}{C_p d}}, \quad (1)$$

210 where  $T$  is the temperature,  $P$  is the pressure,  $P_0$  is the reference pressure (1000 hPa),  $R_d$  is the dry air gas constant and  $C_p d$  is  
 211 the specific heat at constant pressure for dry air.

212 A useful way to identify density currents is with virtual potential temperature  $\theta_v$ , introduced by Lilly (1968). Virtual  
 213 potential temperature takes into account the temperature and moisture content of air and can be used as a proxy for buoyancy. It  
 214 is defined as:

$$\theta_v = \theta(1 + 0.61r - r_L), \quad (2)$$

215 where  $r$  is the mixing ratio of water vapour, and  $r_L$  is the mixing ratio of liquid water. Low  $\theta_v$  indicates dense air, whereas high  
 216  $\theta_v$  indicates buoyant air. Again, this equation was applied to observations and the simulations.

## 217 4 | RESULTS

### 218 4.1 | Synoptic conditions

219 Between 14 and 26 Jan 2019, the Lake Victoria basin (region in Fig. 2a) received almost 50% more rainfall than the 2000–2018  
 220 average for that period (based on GPM). Note that periods of convection are not unusual in this dry season, and this enhancement  
 221 of rainfall was likely due to an active MJO in phases 3 and 4 (Pohl and Camberlin, 2006a,b; Hogan et al., 2015) between 14 Jan and  
 222 21 Jan, as well as a Kelvin wave passage across the region (Schreck n.d., <https://ncics.org/portfolio/monitor/mjo/>).  
 223 By the time of the campaign, the MJO had moved into phase 6, which tends to suppress rainfall activity in the region. However,  
 224 isolated convective events continued to occur over the lake. In particular, significant storms occurred on the three nights preceding  
 225 the first flight.

226 Figure 4 shows climatologies for the two-week period centred on the HyVic flights, conditions during the campaign (26–27  
 227 Jan), and the anomaly from the climatology for East Africa. January and February are technically a dry season, although  
 228 observations show that January and February are only slightly drier than the Short Rains season over the Lake Victoria catchment  
 229 (Yin and Nicholson, 1998). Late January/early February is characterised by high pressure over northern East Africa and lower  
 230 pressure to the south of the region (Fig. 4a). Near-surface (10 m) winds are northeasterly directed along the Somali coastline  
 231 and veer eastward over Kenya toward the Lake Victoria basin (Fig. 4d). Winds at 700 hPa are also easterly across the basin,  
 232 having veered from southerly over the western Indian Ocean (Fig. 4g). For comparison, during July (dry season case study in  
 233 W19) a high pressure ridge extends through Tanzania into Kenya from the south and the northern region is under relatively lower



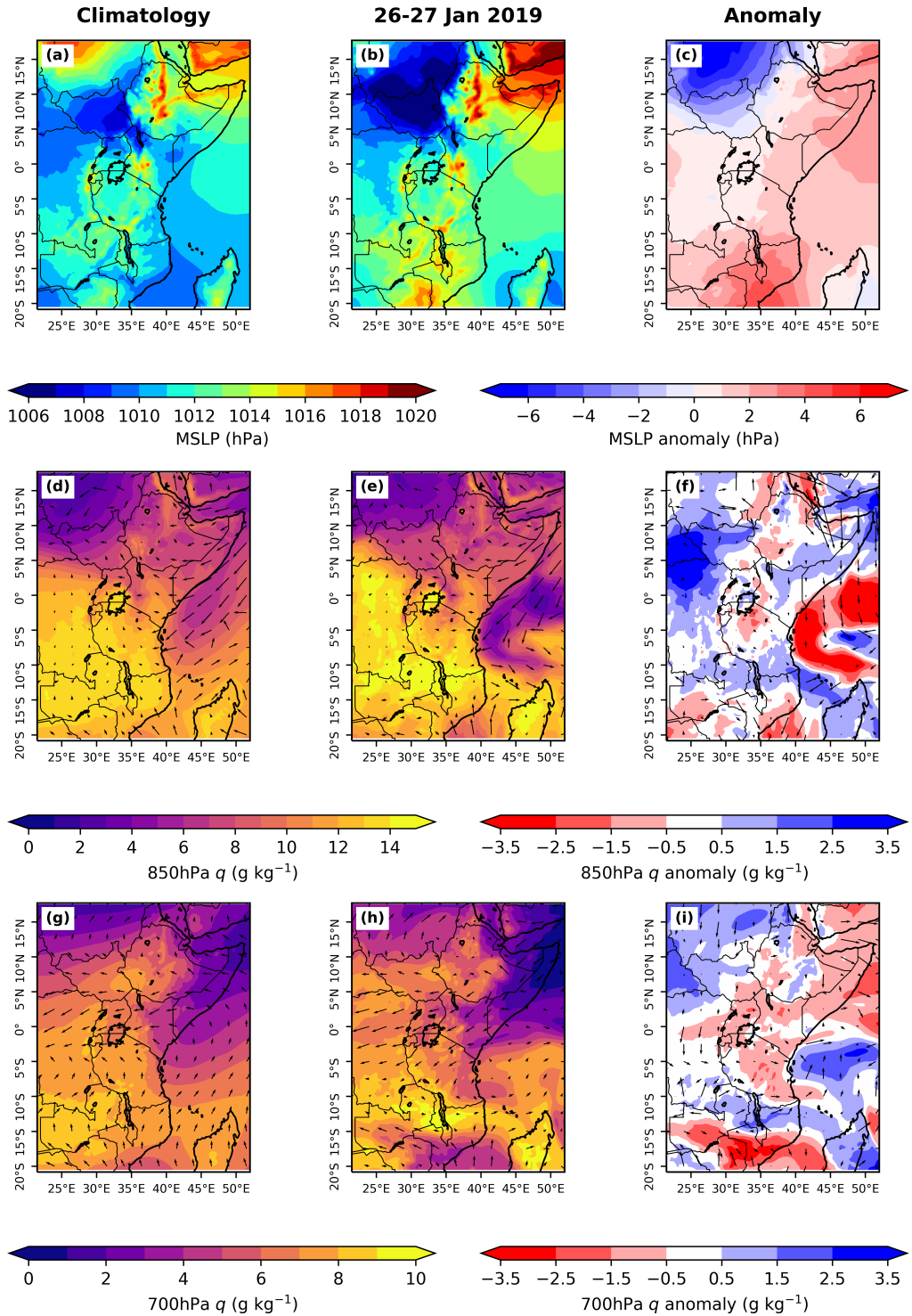


FIGURE 4 Synoptic situation during HyVic flights. (a-c) Mean sea level pressure, (d-f) 850 hPa specific humidity (contours) and 10 m winds (arrows) and (g-i) 700 hPa specific humidity (contours) and 700 hPa winds (arrows). First column shows mean climatology from 1979–2019 for the 2 week period surrounding the HyVic flights (19 Jan–3 Feb 2019), second column shows mean during the HyVic period (26–27 Jan 2019) and third column shows the anomaly from the climatology during the HyVic period. Data from ERA5.

pressure (not shown). Near-surface winds are reversed along the coastline such that they are southeasterly along the Tanzanian coast and south westerly along the Somali coast. Winds over Kenya still veer eastward over the basin, but have an additional southerly component. Winds at 700 hPa are general southerly over the basin, although did have an easterly component during the W19 case study, more similar to January/February.

During the campaign, a stronger than usual surface ridge extended from the Arabian Peninsula across Ethiopia and Somalia and a ridge also extended from the south of the domain to southern Tanzania (Figs. 4a-c). A greater relative increase in pressure over the Arabian Peninsula compared to the Indian Ocean resulted in a greater northerly component of the near-surface winds along the Somali coastline, with correspondingly drier air at 850 hPa over the Indian Ocean (Figs. 4e,f). A region of anomalously low pressure was situated over Sudan during the campaign (Figs. 4b,c), which seemingly had little impact on the circulation over the Lake Victoria basin at 10 m (Figs. 4e,f) or 700 hPa (Figs. 4h,i), although was likely responsible for surface northwesterly flow bringing increased moisture at 850 hPa to the region north west of the lake.

Over the basin itself, the mean winds at 10 m and 700 hPa for the two-day campaign period were almost identical to the climatology (Figs. 4e,f,h,i). In general, specific humidity at 850 hPa was similar to the climatology over the Lake Victoria Basin, although air was  $\sim 1 \text{ g kg}^{-1}$  drier immediately to the east of the lake and  $\sim 1 \text{ g kg}^{-1}$  more moist over the north and west of the lake compared to climatology (Fig. 4f). At 700 hPa, air was  $\sim 1 \text{ g kg}^{-1}$  drier than climatology over large parts of the Lake Victoria Basin and Somalia, related to dry air over the Arabian Peninsula and northern Indian Ocean transported by the northeasterly winds across Somalia. Other than the dry anomaly at 700 hPa, the similarity of the winds and 850 hPa moisture to the climatology suggest that the period is fairly representative for the time of year. ~~However, the two-day mean may mask information on the variability of the diurnal cycle.~~

## 4.2 | Evening flight

Figures 5 and 6 show data along the transects defined in Figs. 3a,b, which are approximately from the northwest to southeast. For the remainder of the paper, 'northwesterly' and 'southeasterly' will be used to describe along-transect winds, but the reader should bear in mind that these descriptions are approximate (the bearing of the transect is  $\sim 120^\circ$ ). Figures 5a,b (black lines) and 5e,f (overlaid track) show that the lake breeze front at  $\sim 300 \text{ m AGL}$  ( $\sim 2000 \text{ m MSL}$ ) was observed between 45–50 km inland from the eastern shore (black dashed line and red x-axis labels) at approximately 1627 LT. The along-transect wind reverses direction across the front, changing from approximately  $+3 \text{ ms}^{-1}$  (northwesterly) to  $-5 \text{ ms}^{-1}$  (southeasterly) over  $\sim 5 \text{ km}$  (Fig. 5a). Over the same distance, specific humidity decreases by  $\sim 6 \text{ g kg}^{-1}$  (Fig. 5b). The specific humidity continues to decrease at a lower rate ahead of the front, in total falling  $\sim 9 \text{ g kg}^{-1}$  over  $\sim 20 \text{ km}$ . At the closest model output time (1600 LT, T+37 h forecast), the lake breeze front is situated in a broadly similar location to the observations for all three model configurations (Figs. 5a,b, coloured lines). The location of the front in the 300 m simulation (green line in Figs. 5a,b, and background of Figs. 5e,f) is  $\sim 3 \text{ km}$  further inland compared to observations. All three model configurations capture the wind reversal and moisture decrease across the front, but the rate of change is too low in the 1.5 and 4.4 km configurations, especially the latter which shows a more gradual change over  $\sim 30 \text{ km}$  (Fig. 5a).

Approximately 15 km offshore ( $\sim 33.88^\circ \text{E}$ , indicated by arrow), the aircraft observations show another sharp front in both wind and moisture (too far behind the lake breeze front to be attributed to the aircraft passing into the head region of the flow). In the direction of the shoreline, specific humidity increases by  $\sim 5 \text{ g kg}^{-1}$ , and the wind increases from nearly stagnant to  $\sim +4 \text{ ms}^{-1}$  (northwesterly). The cause of this front over the lake remains unclear. One hypothesis is that the aircraft passed into a region with deeper lake breeze. A deeper lake breeze is expected inland as a result of the transport of near-surface moisture by turbulent eddies in the convective boundary layer (Reible et al., 1993). A return flow above the lake breeze could have transported some of the lofted moist air back toward the lake at upper levels, with over-lake subsidence returning the moisture to the surface (although no observations are available to test this theory). Deepening of the lake breeze may also occur if the air is decelerated

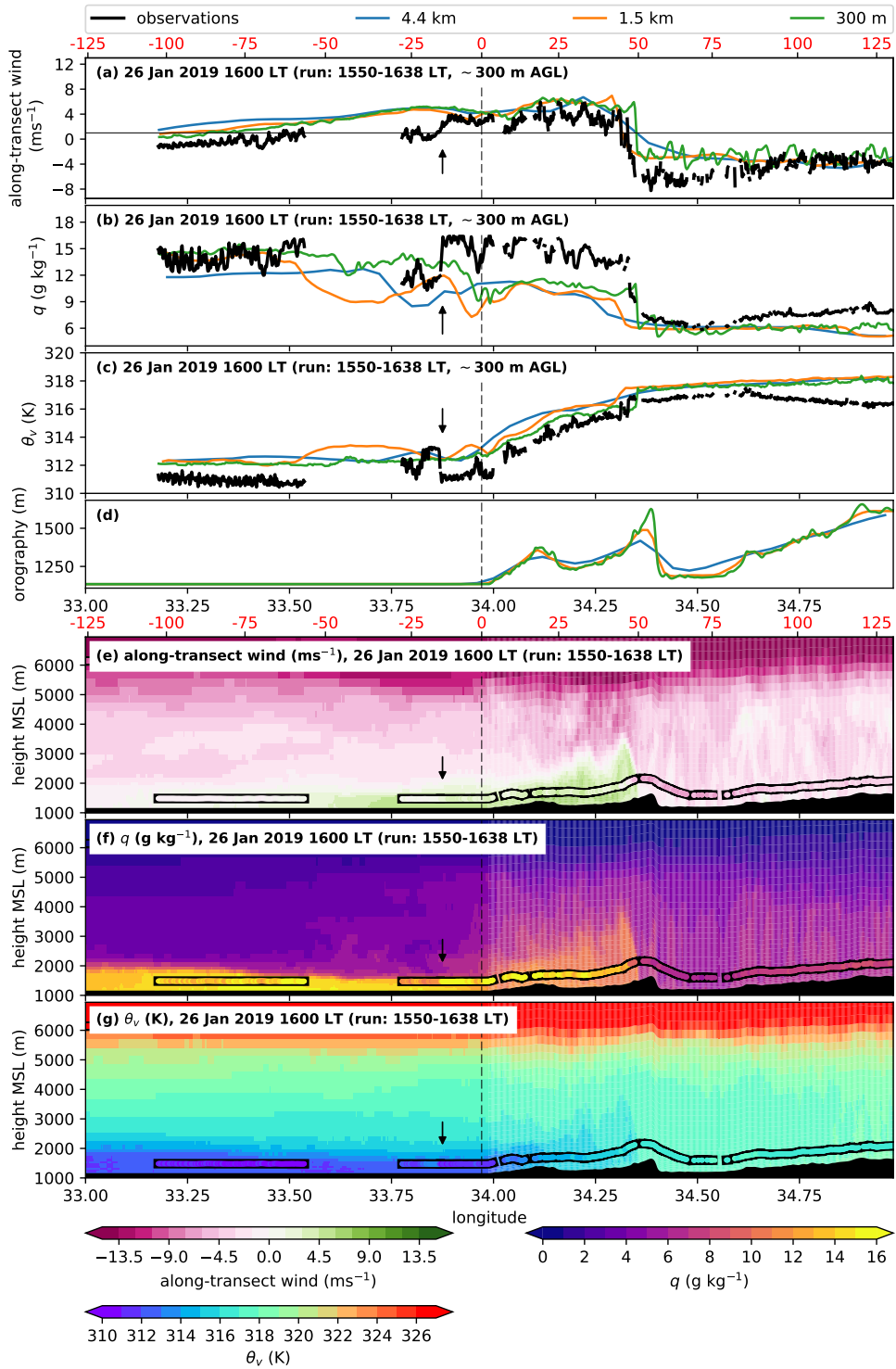


**FIGURE 5** Aircraft observations (black) of (a) along-transect wind and (b) specific humidity and (c) virtual potential temperature along a ~300 m AGL (~1400 m MSL when above the lake) run moving from the lake (northwest) to land (southeast). Simulated variables from CP MetUM with three different resolutions are also plotted (colours), obtained from a virtual fly-through of the model along the aircraft track. (d) Orography from the three model resolutions. Cross-sections of (e) along-transect wind and (f) specific humidity and (g) virtual potential temperature from the aircraft observations. The simulated variables (from the 300 m model) from the closest model output time to the observations are plotted underneath. All plots share the same x-axis (longitude). The distance in km from the eastern shore of the lake (black dashed line) are shown in red. Positive (negative) numbers are onshore (offshore). [Arrows are explained in text.](#)

at lower levels due to increased surface friction (as the flow moves onshore), or if the flow is blocked by the orography, causing it to pile up. However, since the model does not capture the apparent front, it is difficult to comment on the mechanism of its formation. Instead of a jump in magnitude, the model along-transect winds become gradually stronger between  $\sim 100$  km offshore and the lake breeze front, such that their magnitude is similar to observed at the front (Figs. 5a,e). Simulated specific humidity is variable across the lake, but is not enhanced over the leading  $\sim 60$  km of the lake breeze as observed (Figs. 5b,f).

The 300 m model shows a pronounced ‘head’ ( $\sim 10$  km wide) at the leading edge of the lake breeze, which is approximately double the depth of the flow behind (Fig. 5e,f), in agreement with density current theory (Simpson, 1982). Waves can also form and break at the top of a density current head (Simpson, 1982). Figures 5a,b, show oscillations in observed along-transect wind and specific humidity at approximately  $+25$  and  $+35$  km, which could correspond to waves. However, it is more likely that these oscillations correspond to turbulent eddies in the convective boundary layer (BL) over land (Reible et al., 1993), which are responsible for the deepening of the lake breeze over land relative to the lake (Figs. 5e,f).

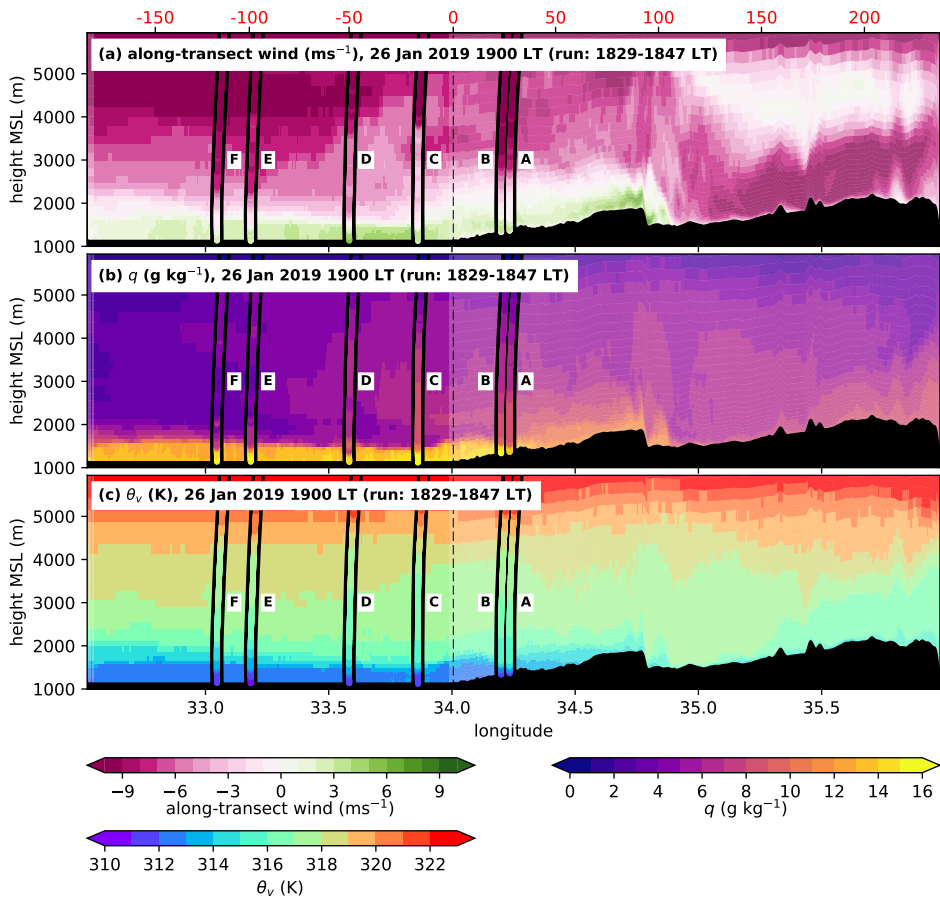


**FIGURE 6** Cross-sections of (a) along-transect wind and (b) specific humidity and (c) virtual potential temperature from the dropsonde observations. The simulated variables (from the 300 m model) from the closest model output time to the observations are plotted underneath. The simulated variables (from the 300 m model) from the closest model output time to the observations are plotted underneath. All plots share the same x-axis (longitude). The distance in km from the eastern shore of the lake (black dashed line) are shown in red. Positive (negative) numbers are onshore (offshore). Note that the transect extends further west and east compared to Fig. 5.

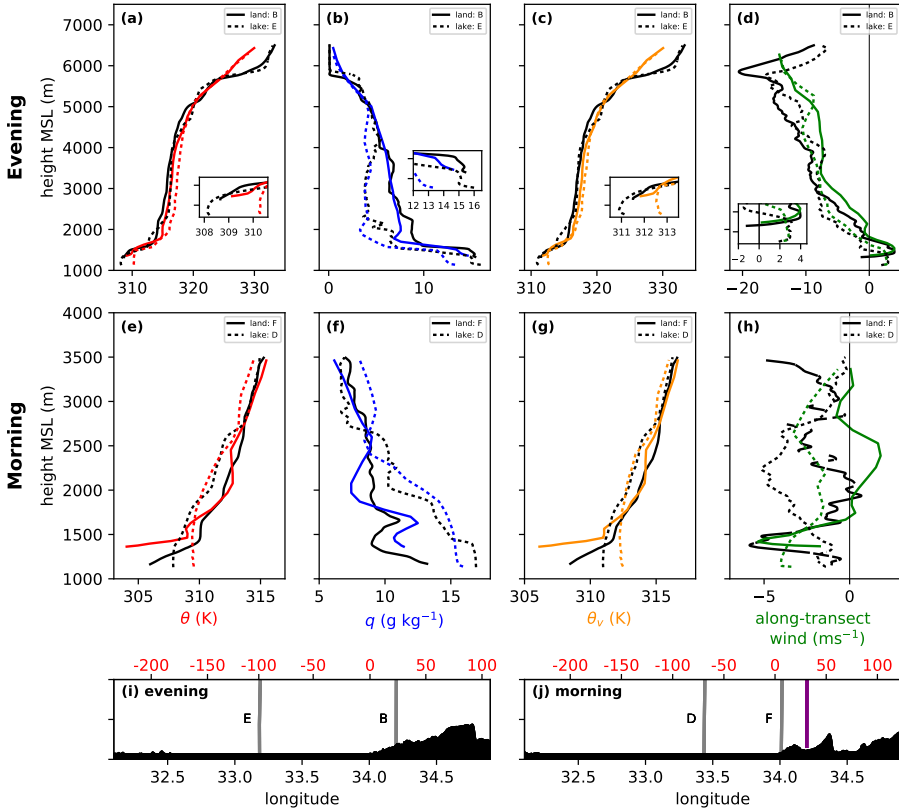


FIGURE 7 Profiles of observed (black, from dropsondes) and simulated (colours, from the 300 m model) (a),(e) potential temperature, (b),(f) specific humidity, (c),(g) virtual potential temperature and (d),(h) along-transect wind (positive winds correspond to northwesterlies) during the (a-d) evening and (e-h) morning flights. Solid lines show profiles over Lake Victoria and dashed lines show profiles over land to the east of the lake. The location of the sonde drops are shown for (i) the evening flight and (j) the morning flight by the black lines. Note the different vertical scales in the first and second row of plots. Inset axes in the top row show a zoom of the lowest 1500 m AGL. Given that the sonde over land during the morning flight was very close to the lake shore, the simulated profile is computed further inland on the purple line in (j). In (i),(j) the distance in km from the eastern shore of the lake is given by the red numbers and the letters correspond to the sonde labels in Figs. 6 and 8.


286 Around 1900 LT, southeasterlies were observed above the northwesterly lake breeze flow in the sonde profiles (**black lines**)  
287 above 1500 m MSL (~350 m AGL) over the lake (**E, dashed line**) and 1750 m MSL (~425 m AGL) over the land (**B, solid**  
288 **line**) (Fig. 7d). The strength of the southeasterly wind increases with height up to ~6 km MSL over both the land and lake,  
289 above which there is a sharp reduction in along-transect wind (**Fig. 6a and Fig. 7d**). Air in this mid-level region (below the free  
290 troposphere) is warmer and drier than the lake breeze layer, but cooler and more moist than the air above, with moisture and  
291 temperature exhibiting a transition between 5.5–6 km MSL, similar to the winds (Figs. 7a-d). This layer of air likely corresponds  
292 to the lake-ward return flow of the lake breeze (Thiery et al. 2015; W19). The models show similar behaviour to the observations  
293 (**e.f. coloured and black lines, Figs. 7a-d**).

294 The return flow can be better visualised from the simulations. At 1600 LT, the 300 m model shows a region of strong  
295 southeasterlies between 3–5 km MSL which extend from the leading edge of the lake breeze back to ~ 15 km onshore (Fig. 5e).  
296 Figure 5f shows enhanced specific humidity in this region, where the return flow advects moisture from the lake breeze—that has  
297 been mixed upwards over land—back over the lake. At this time, no observations were recorded in this return flow region; in  
298 hindsight, the altitude of the mid-level leg designed to sample the return flow (~6 km MSL, 1756-1813 LT) was too high (above  
299 the return flow region identified in Figs. 7a-d).

300 At 1900 LT, the simulated lake breeze front has moved further onshore (~+110 km) and the lake-ward return flow has  
301 extended further back over the lake (Figs. 6a,b). The extent of the return flow is less clear in the along-transect wind than at  
302 1600 LT since the prevailing easterly winds have generally strengthened at all heights across the transect (**e.f. Fig. 5e and Fig.**  
303 **6a**). However, the extended influence of the return flow is clear in the specific humidity, with values  $> 5 \text{ g kg}^{-1}$  extending  
304 approximately 100 km offshore (Fig. 6b). The transect in Fig. 6 is extended further to the east compared to Fig. 5 to show  
305 the land-ward branch of the return flow east of the lake breeze front (reduced south easterlies between 3–5 km MSL east of  
306 +100 km, Fig. 6a). The return flow is clearly visible in sondes A and B over land, with strong southeasterlies and high specific  
307 humidity above ~2.5 km MSL (Figs. 6a,b). Sondes C and D (15 and 35 km offshore respectively) also show enhanced specific  
308 humidity up to ~4.5 km MSL (compared to E and F), but the southeasterlies are reduced compared to A and B. Sondes E and F  
309 both show increased southeasterlies above 2.5 km MSL compared to sondes C and D. The simulation also shows a reduction  
310 in the along-transect wind in the region around sondes C and D and an increase around sondes E and F. It is unclear why the  
311 southeasterly wind is stronger in E and F compared to C and D or why the model and observations exhibit this similar wind  
312 pattern at mid-levels.

313 An interesting feature in the profile from sonde B (over land) is the distinct layer of well-mixed air between ~1500–2200 m  
314 MSL (~350–1050 m AGL) in the transition zone between the lake breeze and return flow (Figs. 7a-c, black solid lines). The  
315 layer is warmer and drier than the lake breeze, but cooler and more moist than the return flow above (Figs. 7a,b). Even in sonde  
316 E (75 km offshore), there is evidence of this well-mixed layer between 1600–2000 m MSL (~350–950 m AGL) (Figs. 7a-c,  
317 black dashed lines). This layer could be a remnant of the lake boundary layer from the previous morning.

318 Along the 300 m AGL transect, cumulus congestus were recorded by an observer on the aircraft, close to where the lake  
319 breeze front was observed over land. Low clouds just onshore of the eastern shore are also visible in the satellite image at 1615  
320 LT (Fig. 3a). By 1645 LT, the congestus in the vicinity of the lake breeze front had developed into deep convection, likely  
321 triggered by convergence at the front. This convection lasted ~1.5 hours, remaining as a small isolated cumulonimbus, before  
322 decaying shortly before sunset. Relatively cold cloud is shown close to the flight track in the satellite image at 1845 LT, likely  
323 remnants of the observed storm (Fig. 3b).

324  In all, the simulations—especially the 300 m horizontal grid-spacing configuration—showed broad agreement with the  
325 observations, which is impressive given the lack of observations available to initialise the model in this region. The aircraft  
326 observations also highlight key biases in the model. Figures 5a-c show that the lake breeze front (at the closest model output  
327 time) was simulated within a few km of the observed front. However, the model snapshot is from approximately 30 minutes  
328 before the aircraft actually crossed the front at 1627 LT, suggesting either that the rate of inland propagation of the front is too

high in the simulation or that the lake breeze initiated earlier in the simulation. The gradient in  $\theta_v$  between the lake and land at 1600 LT is greater in observations than in the model (over the first 75 km onshore, Figs. 5c,g), which would be expected to drive a stronger onshore flow further inland in the observations. The reduced inland propagation may be explained by the stronger southeasterly winds in the 50 km ahead of the lake breeze front compared to the simulations (Figs. 5a,e, +50–+100 km), which offer greater opposition to the propagating lake breeze (Estoque, 1962; Simpson et al., 1977; Arritt, 1993). Figures. 5c,g show decreasing virtual potential temperature  $\theta_v$  was observed eastward of +80 km, whereas simulated  $\theta_v$  shows a small increase. The negative  $\theta_v$  gradient from northwest to southeast in the observations may explain the stronger observed southeasterly winds.

Milton et al. (2017) suggest that only features with a horizontal extent greater than 7 grid-points can be fully resolved in a model. Given the observed width of the lake breeze front, it is not expected that the 4.4 or 1.5 km configurations could accurately simulate this feature. However, the rate of change across the front in the 300 m simulation is too high, corresponding to a reduced horizontal extent of the front compared to observations. The magnitude of change in along-transect wind is too small in all model configurations because the southeasterly winds ahead of the lake breeze front are too weak (discussed above). The magnitude of the change in specific humidity is also too small, although in this case the specific humidity to the east of the lake breeze front is similar to the observations, but the air inside the lake breeze is too dry. This drier lake breeze air will be discussed later in the context of profiles over the lake and land.

Figures 6a,b and Figs. 7a-d show that the depth of the lake breeze (consisting of cooler, moister air and northwesterly winds) at 1900 LT is ~100–200 m greater in the models compared to the dropsonde profiles over both lake and land (e.f. coloured and black lines). In addition, specific humidity within the lake breeze layer is lower in the model than the observations (Figs. 7b, e.f. blue and black lines), despite the model being warmer (Figs. 7a, e.f. red and black lines). This implies that the lake breeze is too dilute in the model as a result of its greater vertical extent. The model is also generally drier than observed immediately above the lake breeze layer (~1600–2200 m MSL, Figs. 7b), suggesting that the deeper lake breeze layer in the model may be caused by excessive entrainment drying at the upper boundary. Given that the near-surface potential temperature is ~2 K warmer in the model than observed over the lake (Fig. 7a, e.f. red and black dashed lines), another contributing factor may be excessive surface heat fluxes in the model, causing exaggerated deepening through turbulent eddies. Note that the observed and modeled near-surface temperatures are very similar between the model and observations over land (Fig. 7a, solid lines), suggesting inadequacies in the representation of the lake surface temperature or the interaction of the lake surface with the atmosphere in the model. It is known that stably stratified BLs are difficult to simulate in numerical models, related to the parametrisation of turbulent diffusion (e.g. Sandu et al. 2013; Holtslag et al. 2013; Fiedler et al. 2013), but further analysis is required to fully address this issue. Goler (2004) showed that sea breezes are deeper when not opposed by environmental winds, so the weaker winds ahead of the lake breeze front may also explain some of the increased lake breeze depth in the simulations.

The deeper lake breeze in the model could explain the missing front at 15 km offshore (discussed above) at 1600 LT since the model is being sampled at a different height relative to the top of the lake breeze air compared to the observations. Therefore, the model was also sampled at heights of 700 and 1000 m above the actual flight path (not shown). At these heights, specific humidity increases between the shore and lake breeze front (all resolutions), but there is no sharp gradient and the increase occurs over land, suggesting there is a feature or interaction which the model cannot correctly simulate.

The representation of the orography of the Lake Victoria basin has been shown to affect circulation and precipitation over the region (e.g. Mukabana and Pielke 1996; Song et al. 2004; Anyah et al. 2006; Finney et al. 2019), therefore it is suggested that differences in the location, gradient and height of the orography in the model may also be responsible for differences between model resolutions and the observations. In particular, the gradient of the orography will affect the strength of anabatic winds which can reinforce the lake breeze. Figure 5d shows how the orographic peak approximately 50 km inland is over 200 m higher in the model configuration with 300 m grid-spacing compared to the configuration with 4.4 km grid-spacing, and occurs ~5 km further inland.



### 4.3 | Morning flight

The along-transect winds, specific humidity and virtual potential temperature  $\theta_v$  measured from the sonde curtain during the morning flight (between 0527-0545 LT) are shown in Figs. 8a-c. Output from the 300 m model is plotted alongside the observations for comparison. Only one sonde (F) was dropped over land, very close to the eastern shoreline. Compared to sondes over the lake, the profile observed by sonde F is much drier, especially near the surface (Figs. 8b and c, ~~black dashed and solid lines in Fig. 7f~~). In the lowest 200 m of sonde F, the observed virtual potential temperature of the air is low (Fig. 8c), and there are strong southeasterly winds between 1300 and 1500 m MSL (150–350 m AGL), suggesting a shallow land breeze across the eastern shoreline (Figs. 8a,c and Fig. 9, ~~brown lines~~). However, this land breeze does not penetrate far offshore (<30 km), shown by the high moisture and increase in  $\theta_v$  near the surface in sonde E (Figs. 8b,c, ~~e.f. brown and purple lines in Fig. 9a~~). There is also no signal of the band of strong southeasterlies between 1300 and 1500 m MSL in sonde E (Fig. 8a, ~~e.f. brown and purple lines in Fig. 9b~~). The offshore extent of the lake breeze (strong southeasterlies and low  $\theta_v$ ) across the eastern shore in the simulation is consistent with the observations (Figs. 8a,c). Sondes D and E show a band of increased southeasterlies between ~1600-2600 m MSL (~450–1450 m AGL), whereas sonde F shows decreased southeasterlies/weak northwesterlies at this level (Fig. 8a and ~~e.f. purple and red lines with brown line in Fig. 9b~~), which could signal a divergent return flow above the land breeze front. Such a return flow is also seen in the model, centred at ~30 km offshore (Fig. 5a). Compared to the dry period case study in W19 (their Fig. 7), the observed position of the convergent land breeze front is much farther east during this flight, suggesting that westward propagation has not occurred or is occurring at a slower rate. This difference in location/propagation could be attributed to the different season or the synoptic situation on that particular day.

Figure 3c shows some relatively warm cloud (>260 K) above the region where sondes D and E were dropped. At this time, solid cloud cover was also reported beneath the aircraft, estimated at ~6000 m MSL. A Skew-T produced by the sonde data (not shown) implies a cloud top of 5550 m MSL. According to GPM IMERG product, there was no rainfall associated with this cloud, although it is likely GPM could have missed light rainfall over such a small spatial extent (GPM is on a grid of 0.1°). However, a precipitating cloud may explain the low  $\theta_v$  air near the lake surface in sonde D (Fig. 8c and Fig. 9a, ~~red line~~).

The simulation produces a land breeze across the western shore which extends 10–15 km offshore (Figs. 8a-c). This region was not sampled by the aircraft or dropsondes. Sonde A (the western-most sonde) recorded near-surface air with lower  $\theta_v$  compared to sondes B and C over the centre of the lake (Fig. 8c and Fig. 9a, ~~e.f. blue line to orange and green lines~~). Low  $\theta_v$  air could indicate a land breeze across the western shore, although this would have had to propagate over 70 km across the lake (against the prevailing wind). In addition, there are no northwesterlies near the surface in sonde A (Fig. 8a and Fig. 9b, ~~blue line~~). A northwesterly anomaly relative to the prevailing flow may have existed, but there is insufficient observational data coverage to support this.

Despite no northwesterlies in sonde A, weak northwesterlies were observed over the lowest ~100 m of sonde B (~~~90 km from the western shore~~), the profile of which also has greater and deeper moisture than the two sondes either side (Figs. 8a,b and Fig. 9b, ~~e.f. orange line with blue and green lines~~). To the east, sonde C recorded stronger southeasterlies at the surface than any other sonde over the lake (Fig. 9b, ~~green line~~). Low-level northwesterlies in sonde B and southeasterlies in sonde C (~~arrows in Fig. 8a~~) show low-level convergence along this line between the two sondes. The increased and deeper moisture in sonde B supports the suggestion of convergence as it indicates near-surface moist air lifted by the resulting vertical motion (Fig. 8b). However, the origin of the convergence is unclear given that the land breezes from the east and west coasts did not reach this part of the lake. It is ambiguous whether the deepened moisture in sonde B could indicate the presence of the bulge feature from W19. In general, the sonde curtain suggests high variability on small spatial scales across the lake, which cannot be explained with the sparse data coverage, but which may be important for cloud formation and, in certain cases, initiation of deep convection.

Following the sonde drops, transects were also flown at ~3000 m and ~1000 m AGL (~4000 m and ~2000 m MSL respectively, Fig. 2d). Clouds were observed along the 1000 m leg, in particular around 32.6°E (where an onboard observer



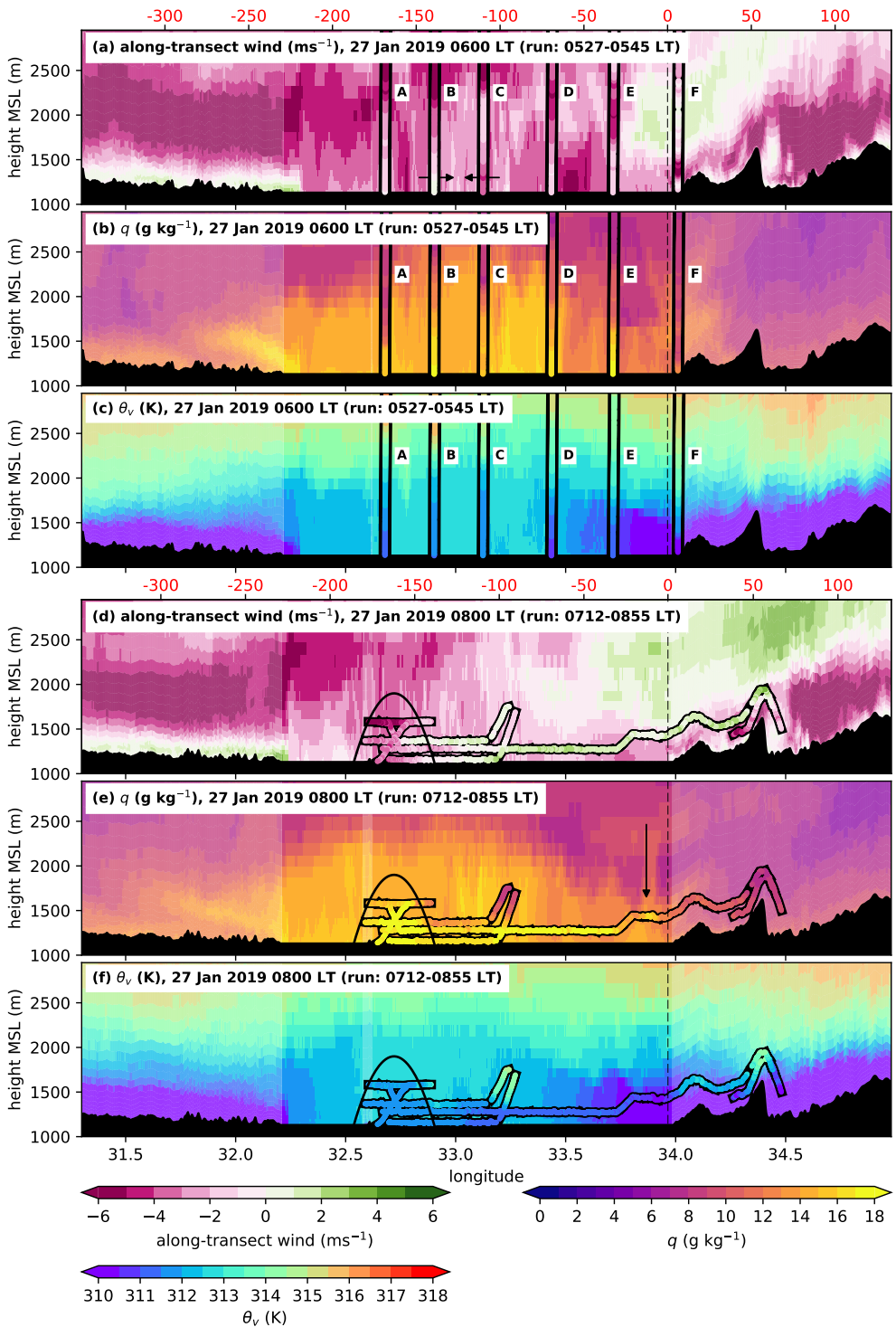


FIGURE 8 Cross-sections of (a),(d) along-transect wind, (b),(e) specific humidity and (c),(f) virtual potential temperature from (a-c) sondes and (d-f) the aircraft. The simulated variables (from the 300 m model) from the closest model output time to the observations are plotted underneath the observations. All plots share the same x-axis (longitude) but the distance in km from the eastern shore of the lake (red numbers) differ between (a-c) and (d-f) due to slightly different flight tracks.

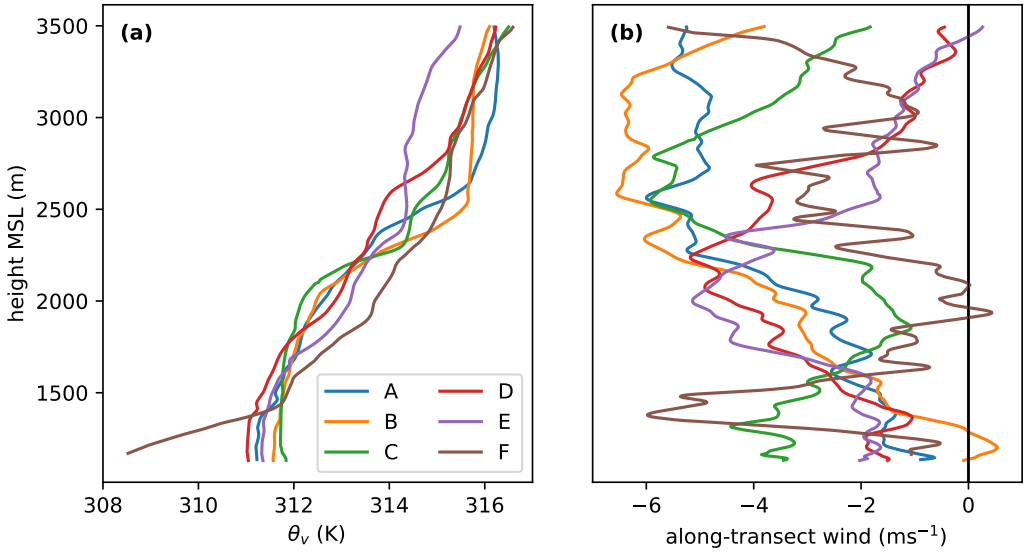


FIGURE 9 (a) Virtual potential temperature and (b) along-transect wind profiles measured by sondes during the morning flight. Positive winds correspond to northwesterlies. The letters correspond to the labels in Fig. 8.

413 reported the cloud base to be approximately 50 m below the aircraft, and the surface of the water beneath was noted to be  
 414 ‘rippled’) and 33.5°E (where the aircraft entered cloud). Figure 3c also shows two regions of low cloud over the lake (one to the  
 415 west and one to the east) corresponding to the observed locations on the track.

Altitude (m)	Subplot	$\sigma$ inside bulge ( $\text{ms}^{-1}$ )	$\sigma$ outside bulge ( $\text{ms}^{-1}$ )
1157	8	0.26	0.20
1278	7	0.29	0.22
1365	6	0.26	0.12

TABLE 2 Standard deviation  $\sigma$  of vertical velocity perturbation  $w'$  inside and outside the bulge regions marked by the solid and dashed lines respectively in Fig. 10. The subplot refers to the numbered inset axes in Fig. 10.

416 Figures 8d-f show aircraft observations from low-level flying between approximately 0700 and 0900 LT. Along the transect  
 417  $\sim 300$  m AGL ( $\sim 1450$  m MSL), two regions of increased specific humidity—possible bulge features—are located at  $\sim 33.9^\circ\text{E}$   
 418 (under arrow in Fig. 8e) and  $\sim 32.75^\circ\text{E}$  (under parabola in Figs.8d-f), where measurements exceeding  $17 \text{ g kg}^{-1}$  were taken.  
 419 These approximately correspond to the locations where clouds were observed on the 1000 and 3000 m AGL legs (although  
 420 there will be some difference given the time delay between the various legs). Note that the model also simulates two bulges of  
 421 enhanced moisture (between  $32.3\text{--}32.5^\circ\text{E}$  and between  $33.0\text{--}33.1^\circ\text{E}$ ), within the lake BL. However, it is unclear whether these  
 422 correspond to the observed bulges given the very different winds in the model and observations (discussed later). Given time  
 423 constraints of the flight, the eastern bulge was sampled at just one height. The western bulge was chosen to be sampled in detail  
 424 because, according to W19 (their Figs. 7j-1 and 14d-f), the bulge would be expected over the western half of the lake at this  
 425 time. Between  $32.6\text{--}32.9^\circ\text{E}$ , the BL was sampled at four heights (between  $\sim 30\text{--}500$  m AGL) and along two profiles. Around  
 426  $32.8^\circ\text{E}$ , specific humidity exceeding  $17 \text{ g kg}^{-1}$  extended to a depth of at least 500 m AGL ( $\sim 1650$  m MSL). At the same height

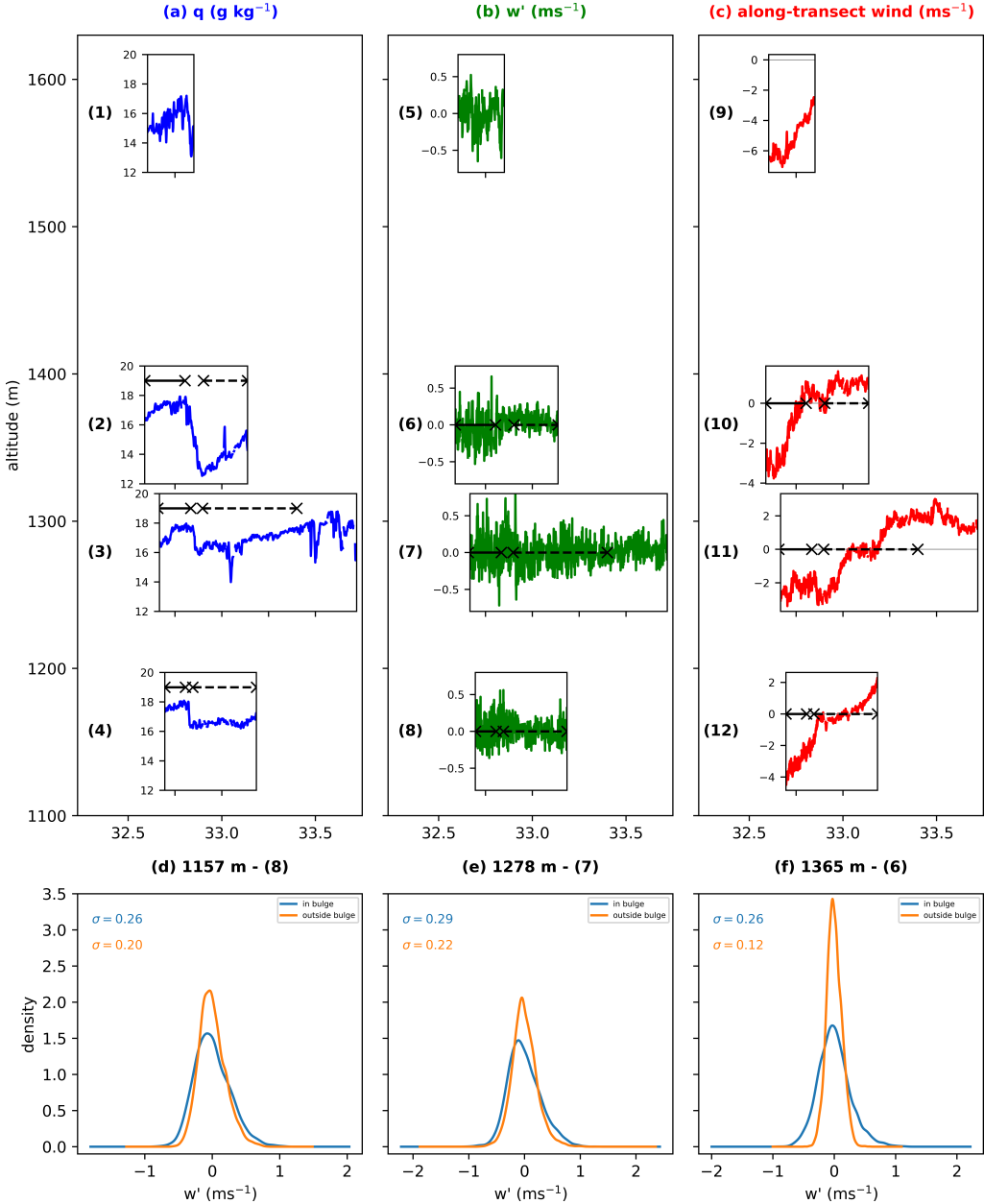


FIGURE 10 (a) specific humidity  $q$ , (b) vertical velocity perturbation  $w'$  and (c) (c) along-transect wind along over-lake transects at the altitudes and longitudes of the inset axes. Regions of negative gradient of the lines in (e-h) correspond to along-transect convergence. The 'bulge' identified in chapter 4 section 4.3, lies approximately to the west of 32.9°E. (d-e) Probability density plots of  $w'$  inside and outside the identified bulge region. The regions marked by the solid (dashed) black lines in the inset axes of (a-c) show the regions inside (outside) the bulge in (d-f).

at 33.25°E (~ 60 km east of the bulge), specific humidity of only 8-10 g kg<sup>-1</sup> was recorded. The along-transect horizontal extent of the high moisture decreases with height, suggesting a dome shape (Fig. 8e).

Figure 8 shows measurements of the specific humidity, vertical velocity perturbation  $w'$  (a proxy for turbulent kinetic energy) and along-transect wind sampled along the transect at different heights within and to the east of the bulge region. The inset axes (numbered) are centred vertically at the mean altitude of each aircraft run and extend horizontally for the length of the run such that all inset axes share the same x-axis (longitude). Data are only shown along straight level runs. The bulge was identified by a sharp increase in specific humidity close to 32.9°E for the three transects below 1500 m MSL (inset axes 2-4). Regions inside the bulge are marked by a straight line and regions immediately outside the bulge are marked by a dashed line in the inset axes of Fig. 10. A visual inspection of the data suggests that  $w'$  is more variable inside the bulge compared to outside (Fig. 10b, inset axes 6-8). Calculation of the standard deviation of  $w'$  shows higher variance inside the bulge at all heights (Table 2), indicating that turbulence is increased inside the bulge. Increased turbulence inside the bulge region likely explains the 'rippled' surface of the water noted at 0650 LT by an observer on the aircraft. The most noteworthy difference in standard deviation of  $w'$  occurs at 1365 m MSL (sim230 m AGL, inset axis 6), where the standard deviation outside the bulge (0.12 ms<sup>-1</sup>) is less than half compared to inside the bulge (0.26 ms<sup>-1</sup>). The standard deviation of  $w'$  outside the bulge at 230 m AGL is also around two times lower than the samples both inside and outside the bulge along the two lower transects. The similar TKE characteristics of the air inside the bulge at 230 m AGL compared to the air at lower altitudes strongly supports the hypothesis that the boundary layer is the source of the air which forms the bulge. The presence of this region of boundary layer air next to a region of quiescent air—likely free-tropospheric air—at 230 m AGL suggests that the the boundary layer air has been lifted upward by a process other than normal overturning, implying convergence at low levels.

Based on W19 (their Figs. 7e,f), southeasterly flow (consisting of prevailing winds, land breeze and katabatic flow) would be expected over most of the lake at the time of these transects, possibly with some convergence close to the (north)western shore due to a land breeze from the northwest. Indeed, this wind pattern is also simulated by the 300 m model during the flight period. However, northwesterlies (green shading) were generally observed to the east of the western bulge, and southeasterlies (pink shading) were observed inside the bulge, indicating large-scale divergence along this transect across the lake surface (Fig. 8d). While divergence across the lake occurs between 2–3 km MSL in the W19 simulation, this is related to a return flow above the low-level convergence (their Fig. 7f). Given that divergence was observed at just 30 m AGL during the flight (Fig. 10e), it is highly unlikely that the aircraft was sampling a return flow at this height. It is unclear whether a land breeze persisted across the western shore at this time, since the aircraft did not fly far enough west to sample this region, but no land breeze was detected at the western-most extent of the low-level transects (approximately 30 km east of the western shore) at 30 and 150 m AGL (Figs. 8d,f and Figs. 10a(3,4)).

The mechanism for the formation of the moisture bulge in W19 is clearly related to large-scale low-level convergence which propagates westward across the lake during the night, lofting near-surface moisture upward and with southeasterlies in its wake. In W19, the convergence occurs to the west of the bulge region, so it is likely that the aircraft track did not extend far enough west to capture the convergent region. However, this does not account for the suppressed upward motion inside the bulge or the northwesterlies to the east. One possibility is that the observed divergence shows the formation of the lake breeze very early in the day, while the signal of elevated moisture produced by possible overnight convergence persists into the morning. Note that sunrise was at 0659 LT, so the lake breeze would have had to form almost immediately after surface warming began. Datta (1981) showed that the land breeze tends to be strongest between 0600 and 0900 LT (although this is likely to vary based on prevailing winds and other synoptic conditions), so the formation of the lake breeze at this time would be unusual. In the model, the divergent lake breeze does not begin to form until 1300 LT (not shown). Another possible explanation for the divergence to the east of the bulge is that it was triggered by convergence to the east earlier in the night and then propagated away from its source region, exhibiting wave-like characteristics; if the wave were propagating westward, then divergence would be expected in its wake.

A further suggestion is that the small-scale convergence shown between sondes B and C in Fig. 8a caused a bulge feature to form. This idea is supported by the deeper moisture in sonde B (Fig. 8b). Figure 10a shows along-transect wind measured along the runs over the lake. Sections of the runs with a negative gradient of along-transect wind indicate wind decelerating toward the northwest, therefore convergence along the transect. In several of the transects, convergence occurs over a horizontal extent of ~10 km (marked by arrows) slightly to the east of the bulge, the eastern edge of which is located around 32.9°E, (identified in specific humidity, Fig. 10a). It is unclear whether this small region of convergence could be responsible for the observed bulge. The small scale of this convergent region again suggests that small-scale perturbations occur over the lake, for which the processes responsible are unknown, but which may be important for cloud and convection formation.

The moist layer above the lake in the model is approximately double the depth of the observations (differences of ~1000 m) and has a less well-defined boundary at the top (Figs. 8b,e, 7e-h (e.f. coloured and black dashed lines)). The water content of the BL is lower in the model than observations (Fig. 7f, e.f. blue and black dashed line). Fig. 7e shows that the potential temperature in the model is warmer by just under 2 K compared to the observations at the surface (e.f. red and black dashed lines), suggesting increased surface heat fluxes may be responsible for the deeper BL, likely attributed to a warmer lake surface. However, issues with the parametrisation of sub-grid mixing in the model may also play a role.

## 5 | CONCLUSIONS

A pilot field campaign using the FAAM BAe-146 aircraft to sample the lake–land breeze circulation over Lake Victoria successfully carried out two flights, observing the lake and land breezes at their respective times in the diurnal cycle in unprecedented detail. Notably, this campaign provides the first observations of the vertical structure of the lake–land breeze circulation. The observational period was generally dry, allowing the baseline lake–land breeze circulation to be observed without the complicating impacts of storm circulations. High-resolution CP MetUM simulations were performed for the HyVic period. Model evaluation was performed and, where appropriate, the simulations were used to fill gaps in the aircraft data. In particular, this novel observational data set provides the first observational evidence to back up the model simulations from Woodhams et al. (2019).

During the evening flight, the aircraft sampled the lake breeze across the eastern shore at a height of ~300 m AGL, traversing the lake breeze front at 1627 UTC approximately 50 km onshore. The lake breeze front exhibited a wind reversal in which the velocity changed by ~8 ms<sup>-1</sup> and specific humidity decreased by 6 g kg<sup>-1</sup> over just 5 km. A return breeze layer between 2–5 km MSL (1–4 km AGL) was identified in dropsonde profiles between 1829–1843 UTC, showing that moist air—likely advected over land by the lake breeze—had been transported back toward the lake at mid-levels, extending at least 50 km offshore. A small isolated cumulonimbus was observed to form around 1700 LT in the region of the lake breeze front, with an estimated life cycle of 1.5 hours.

The main aim of the morning flight was to identify any land breezes and investigate the potential existence of a bulge of moist air over the lake surface identified in simulations in W19. During the flight, a land breeze with a depth of 350 m was observed in a dropsonde profile close to the eastern shore at 0545 LT, penetrating no further than 30 km offshore. It is unclear how long this land breeze persisted. Sonde drops over the lake during the early morning showed high variability in wind, moisture and temperature between adjacent sondes, despite the drops being spaced only 25–50 km apart. The details and causes of this variability cannot be deduced given the limited data coverage. An isolated region of convergence and elevated moisture was identified around 32.9°E, almost directly over the centre of the lake, but the cause is unclear due to the limited coverage of the dropsondes and the minimal propagation of the land breeze across the lake.

Between 0700–0900 LT, a significant region of elevated moisture (possibly related to the elevated moisture identified in the dropsonde profiles) was identified between 32.6–32.9°E (~70 km west of the western shore) and sampled by the aircraft at

various heights between 30–500 m AGL and along two profiles. Specific humidity exceeding  $17 \text{ g kg}^{-1}$  was observed to a depth of at least 500 m AGL at  $32.8^\circ\text{E}$  compared to  $8\text{--}10 \text{ g kg}^{-1}$  at the same height 60 km to the east. In W19, this region of elevated moisture—with a depth between a few hundred metres and  $1 \text{ km}$ —was related to convergence over the lake, partly due to land breezes. The aircraft was unable to sample to the west of the bulge, so the convergence likely responsible for the formation of the bulge could not be investigated. Northwesterly winds were observed at all levels (as low as 30 m AGL) to the east of the bulge region, at a time when southwesterlies were expected across the whole lake. Turbulence was shown to increase inside the bulge region and there were visible disturbances to the surface of the lake.

Convection-permitting MetUM was run for the period at three different horizontal grid-spacings: 4.4 km, 1.5 km and 300 m. The model was able to reproduce key features and processes, such as the lake breeze front, in terms of timing and location with reasonable accuracy, which is a major achievement due to the lack of observations assimilated in this region. However, the width of the lake breeze front was too great in the 4.4 and 1.5 km configurations and too narrow in the 300 m model. For example, at a horizontal grid-spacing of 4.4 km—the configuration of the current operational CP MetUM model over tropical Africa run by the UK Met Office—the lake breeze front had a width of  $\sim 30 \text{ km}$ . Differences between model configurations and observations may be related to surface temperatures—in particular the near-surface temperature over the lake is too warm—as well as differences in the representation of orography. In all model configurations, the depth of the simulated lake breeze was too great, causing dilution of the moisture in this layer. Similarly, the simulated depth of the BL over the lake during the morning flight was too deep and near-surface specific humidity too low. Again, these differences could be attributed to a warmer lake surface in the model generating excessive surface fluxes and over-deepening the BL. Deficiencies in the parametrisation of sub-grid mixing likely also play a role.

Although it is difficult to draw robust conclusions from just two flights, the HyVic pilot flight campaign has provided direction and motivation for a future extended aircraft campaign over the region, demonstrating proof of concept that key processes can be observed. Such a campaign should include increased sampling near the surface and a higher density of sonde drops to observe and understand small-scale variability over the lake. Aircraft can sample at many levels, but the atmosphere may quickly evolve between different legs, which makes it difficult to attribute differences to time or location. Accordingly, ground observations—including automatic weather stations (AWSs), wind profilers, doppler lidars and radiometers—are required in conjunction with the aircraft. An ideal tool—both for scientific study and operational forecasting—would be radar, which can complete a 3D scan within a relatively small time window, such that multiple scans can be used to study the 3D evolution of the circulations or storm structure. First radar observations from the S-band dual-polarised radar in Mwanza (southern shore of Lake Victoria) operated by the Tanzania Meteorological Agency have been presented by Waniha et al. (2019), demonstrating the utility of the radar to identify convergence lines over the lake.

In addition to more observations, idealised modelling will be a useful tool to study the moisture bulge during the early morning. Simulations of lake breeze collisions under different environmental conditions—such as environmental humidity, prevailing wind and land–lake temperature contrasts—could be used to understand the formation of the bulge, as well as conditions under which it contributes to storm formation over Lake Victoria. An open question—especially given the northwesterly winds observed to the east of the moisture bulge in this campaign—is whether the propagation of the bulge feature is controlled by density current or wave dynamics. It has been shown that even high-resolution models struggle to correctly simulate the wind, moisture and temperature gradients across the lake breeze front. It is important to understand how this gradient may affect the known triggering of storms within the convergence zone of the lake breeze front. Idealised modelling could also address this question by performing simulations with different horizontal grid-spacings, or by artificially imposing synoptic conditions or lake–land contrasts to change the strength of the lake breeze front.

A major problem in the representation of the lake–land breeze circulation and associated features in the models was the overestimation of the depth of the boundary layer, which also resulted in dilution of the moisture content. Sensitivity studies are required to investigate sub-grid mixing in the BL. Inaccurate lake surface temperatures may also play a role, by affecting surface

fluxes and temperature contrasts between the lake and land. The latter likely affects the strength and timing of lake and land breezes too. Sensitivity analysis to lake surface temperatures could be performed by artificially changing the input temperatures from the OSTIA analysis used to define the water temperatures in the model (Fiedler et al., 2014). The lake surface temperatures in the model are only updated once per day, so the effect of applying a diurnally varying temperature perturbation should be investigated. Rooney and Bornemann (2013) previously coupled the FLake model (Mironov, 2008; Mironov et al., 2010) to the MetUM UKV configuration over the UK and showed some modification of local weather, while FLake has previously been used over the African Great Lakes by Thiery et al. (2014, 2015).

Given the devastating impacts of storm occurrence over the lake, improving understanding of the processes responsible for storm initiation is key to improving safety on the lake. HyVic has provided observations of the [baseline](#) lake–land breeze circulation in unprecedented detail, but an extended campaign is necessary for better statistics and greater observational coverage. In particular, it remains unclear how properties of the lake breeze front and nocturnal moisture bulge may vary on seasonal and synoptic timescales, and how such variations may lead to deep convection, therefore observations are required throughout the year.

## 6 | ACKNOWLEDGEMENTS

The HyVic pilot flight campaign was only possible because of true collaboration and cooperation between a multitude of projects and funding bodies. Many thanks to the PIs of the various projects involved for working together to deliver the campaign at such low cost. Airborne data was obtained using the BAe-146-301 Atmospheric Research Aircraft (ARA) flown by Airtask Ltd and managed by FAAM Airborne Laboratory, jointly operated by UKRI and the University of Leeds. Many thanks to various members of FAAM for their help and guidance during the campaign. Flight hours were provided by the National Centre for Atmospheric Science (NCAS) and the UK Met Office. This research was conducted with financial support from UKAID under the WISER Programme through the HIGHWAY (HIGH impact Weather LAke sYstem) Project. The HIGHWAY project is an international collaboration led by the WMO, in cooperation with Kenya Meteorological Department, Meteo Rwanda, Uganda National Meteorological Authority, Tanzanian Meteorological Agency, UK Met Office and National Centre for Atmospheric Research, USA. This work was also supported by U.K. Research and Innovation as part of the Global Challenges Research Fund, Grant NE/P021077/1 (GCRF African SWIFT). This work was also supported by the U.K. Department for International Development (DFID)/Natural Environment Research Council (NERC) Future Climate for Africa (FCFA) HyCRISTAL project (NE/M019985/1). Woodhams was also supported by the NERC SPHERES DTP (Grant NE/L010627/1). Marsham was also supported by the National Centre for Atmospheric Science via the NERC/GCRF programme ACREW: Atmospheric hazard in developing Countries: Risk assessment and Early Warning. Thanks are owed to Festus Luboyera, Solomon Mangeni and others at Uganda National Meteorological Authority (UNMA) for their hard work in ensuring HyVic could take place. Thank you and credit to the NERC Methane Observations and Yearly Assessments (MOYA) project for funding the transits and supporting HyVic as an addition to their campaign. ERA5 data were generated using Copernicus Climate Change Service Information (2020). Neither the European Commission nor ECMWF are responsible for any use that may be made of the Copernicus Information or data in this publication.

## REFERENCES

- Grant Allen, Joseph Robert Pitt, Keith Bower, Tom Bannan, James D Lee, Patrick Barker, Prudence Bateson, James R Hopkins, Rebecca Fisher, David Lowry, et al. MOYA Aircraft Campaigns: Highlights from the Methane Observations and Yearly Assessment Project Aircraft Campaigns in Africa and the Arctic. *AGUFM*, 2019:B13J–2423, 2019.
- Richard O Anyah, Fredrick HM Semazzi, and Lian Xie. Simulated physical mechanisms associated with climate variability over Lake

- 592 Victoria Basin in East Africa. *Mon. Wea. Rev.*, 134(12):3588–3609, 2006.
- 593 Raymond W Arritt. Effects of the large-scale flow on characteristic features of the sea breeze. *Journal of Applied Meteorology*, 32(1):  
594 116–125, 1993.
- 595 Mamoudou B Ba and Sharon E Nicholson. Analysis of convective activity and its relationship to the rainfall over the Rift Valley lakes  
596 of East Africa during 1983-90 using the Meteosat infrared channel. *J. Appl. Meteor.*, 37(10):1250–1264, 1998.
- 597 Patrick A Barker, Grant Allen, Thomas Bannan, Archit Mehra, Keith N Bower, Joseph R Pitt, Stéphane J-B Bauguitte, Dominika  
598 Pasternak, Rebecca E Fisher, James D Lee, et al. Airborne measurements of fire Emission Factors for African biomass burning  
599 sampled during the MOYA Campaign. *Atmospheric Chemistry and Physics Discussions*, pages 1–37, 2020.
- 600 KM Beswick, MW Gallagher, AR Webb, EG Norton, and F Perry. Application of the Aventech AIMMS20AQ airborne probe for  
601 turbulence measurements during the Convective Storm Initiation Project. *Atmospheric Chemistry and Physics*, 8(17):5449–5463,  
602 2008.
- 603 M Bush, T Allen, C Bain, I Boutle, J Edwards, A Finnenkoetter, C Franklin, K Hanley, H Lean, A Lock, et al. The first Met Office  
604 Unified Model/JULES Regional Atmosphere and Land configuration, RAL1. *Geosci. Model Dev. Discuss.*, 2019.
- 605 Terry Cannon, Fred Krüger, Greg Bankoff, and Lisa Schipper. Putting culture at the centre of risk reduction. In Terry Cannon and Lisa  
606 Schipper, editors, *World Disasters Report 2014: focus on culture and risk*, pages 185–209. International Federation of Red Cross  
607 and Red Crescent Societies, 2014.
- 608 JM Chamberlain, CL Bain, DFA Boyd, K McCourt, T Butcher, and S Palmer. Forecasting storms over Lake Victoria using a high  
609 resolution model. *Meteor. Appl.*, 21(2):419–430, 2014.
- 610 Copernicus Climate Change Service (C3S). ERA5: Fifth generation of ECMWF atmospheric reanalyses of the global  
611 climate. Copernicus Climate Change Service Climate Data Store (CDS). Last accessed: 1 May 2020. URL:  
612 <https://cds.climate.copernicus.eu/cdsapp#!/home>. 2017.
- 613 RR Datta. Certain aspects of monsoonal precipitation dynamics over Lake Victoria. In James Lighthill and Robert Pearce, editors,  
614 *Monsoon Dynamics*, pages 333–349. Cambridge University Press, 1981.
- 615 Mariano A Estoque. The sea breeze as a function of the prevailing synoptic situation. *Journal of the Atmospheric Sciences*, 19(3):  
616 244–250, 1962.
- 617 Emma K Fiedler, Matthew J Martin, and Jonah Roberts-Jones. An operational analysis of lake surface water temperature. *Tellus A*, 66  
618 (1):21247, 2014.
- 619 S Fiedler, K Schepanski, B Heinold, P Knippertz, and I Tegen. Climatology of nocturnal low-level jets over North Africa and implica-  
620 tions for modeling mineral dust emission. *J. Geophys. Res.: Atmospheres*, 118(12):6100–6121, 2013.
- 621 Declan L Finney, John H Marsham, Lawrence S Jackson, Elizabeth J Kendon, David P Rowell, Penelope M Boorman, Richard J Keane,  
622 Rachel A Stratton, and Catherine A Senior. Implications of improved representation of convection for the East Africa water budget  
623 using a convection-permitting model. *Journal of Climate*, 32(7):2109–2129, 2019.
- 624 Declan L Finney, John H Marsham, Dean P Walker, Cathryn E Birch, Beth J Woodhams, Lawrence S Jackson, and Sam Hardy. The  
625 effect of westerlies on East African rainfall and the associated role of tropical cyclones and the Madden–Julian Oscillation. *Quarterly*  
626 *Journal of the Royal Meteorological Society*, 146(727):647–664, 2020.
- 627 Heemakn Flohn and Klaus Fraedrich. Tagesperiodische zirkulation und niederschlagsverteilung am Victoria-See (Ostafrika) (The daily  
628 periodic circulation and distribution of rainfall over Lake Victoria, in German). *Meteorologische Rundschau*, 19(6):157–165, 1966.
- 629 RA Goler. *Numerical model of cloud lines over Cape York Peninsula*. PhD thesis, Ph. D. thesis, Centre for Dynamical Meteorology and  
630 Oceanography, Monash University, 210pp, 2004.



- 631 KE Hanley, JS Pirret, CL Bain, AJ Hartley, HW Lean, S Webster, and Woodhams BJ. Assessment of convection-permitting versions of  
632 the Unified Model over the Lake Victoria basin region. *Quarterly Journal of the Royal Meteorological Society*, in review.
- 633 D. A. Hastings and P. K. Dunbar. Global Land One-kilometer Base Elevation (GLOBE) digital elevation model, documentation, volume  
634 1.0. Key to Geophysical Records Documentation (KGRD), Doc. 34, National Oceanic and Atmospheric Administration, National  
635 Geophysical Data Center. Available at: <https://repository.library.noaa.gov/view/noaa/13424>, 1999.
- 636 Hans Hersbach, Bill Bell, Paul Berrisford, Shoji Hirahara, András Horányi, Joaquín Muñoz-Sabater, Julien Nicolas, Carole Peubey,  
637 Raluca Radu, Dinand Schepers, et al. The ERA5 global reanalysis. *Quarterly Journal of the Royal Meteorological Society*, 146  
638 (730):1999–2049, 2020.
- 639 Emily Hogan, Ann Shelly, and Prince Xavier. The observed and modelled influence of the Madden–Julian Oscillation on East African  
640 rainfall. *Meteor. Appl.*, 22(3):459–469, 2015.
- 641 AAM Holtslag, Gunilla Svensson, P Baas, S Basu, B Beare, ACM Beljaars, FC Bosveld, J Cuxart, Jenny Lindvall, GJ Steeneveld, et al.  
642 Stable atmospheric boundary layers and diurnal cycles: challenges for weather and climate models. *Bull. Amer. Meteor. Soc.*, 94  
643 (11):1691–1706, 2013.
- 644 George J Huffman, David T Bolvin, Dan Braithwaite, Kuolin Hsu, Robert Joyce, Christopher Kidd, Eric J Nelkin, S Sorooshian, J Tan,  
645 and Pingping Xie. Algorithm Theoretical Basis Document (ATBD) Version 06. NASA Global Precipitation Measurement (GPM)  
646 Integrated Multi-satellitE Retrievals for GPM (IMERG). Technical report, Available at: [https://docsserver.gesdisc.eosdis.  
647 nasa.gov/public/project/GPM/IMERG\\_ATBD\\_V06.pdf](https://docsserver.gesdisc.eosdis.nasa.gov/public/project/GPM/IMERG_ATBD_V06.pdf), 2019a.
- 648 GJ Huffman, EF Stocker, DT Bolvin, EJ Nelkin, and J Tan. GPM IMERG Final Precipitation L3 Half Hourly 0.1 degree x 0.1 degree  
649 V06, Greenbelt, MD, Goddard Earth Sciences Data and Information Services Center (GES DISC), Last accessed: 2 Sep 2019, DOI:  
650 10.5067/GPM/IMERG/3B-HH/06. 2019b.
- 651 Douglas K Lilly. Models of cloud-topped mixed layers under a strong inversion. *Quart. J. Roy. Meteor. Soc.*, 94(401):292–309, 1968.
- 652 FE Lumb. Topographic influences on thunderstorm activity near Lake Victoria. *Weather*, 25(9):404–410, 1970.
- 653 Sean Milton, Aida Diongue-Niang, Benjamin Lamptey, Caroline Bain, and Cathryn Birch. Numerical Weather Precition over Africa.  
654 In Douglas J Parker and Mariane Diop-Kane, editors, *Meteorology of tropical West Africa: The forecasters' handbook*, chapter 10,  
655 pages 380–422. John Wiley & Sons, 1 edition, 2017.
- 656 Dmitrii Mironov, Erdmann Heise, Ekaterina Kourzeneva, Bodo Ritter, Natalia Schneider, and Arkady Terzhevik. Implementation of the  
657 lake parameterisation saheme FLake into the numerical weather prediction model COSMO. *Boreal Environ. Res.*, 15(2):218–230,  
658 2010.
- 659 Dmitrii V Mironov. Parameterization of lakes in numerical weather prediction. Part 1: Description of a lake model. Technical  
660 report, Consortium for Small-Scale Modelling. Available at [http://www.cosmo-model.org/content/model/documentation/  
661 techReports/docs/techReport11.pdf](http://www.cosmo-model.org/content/model/documentation/techReports/docs/techReport11.pdf), 2008.
- 662 Andrew K Mirza, Susan P Ballard, Sarah L Dance, Paul Maisey, Gabriel G Rooney, and Edmund K Stone. Comparison of aircraft-  
663 derived observations with in situ research aircraft measurements. *Quarterly Journal of the Royal Meteorological Society*, 142(701):  
664 2949–2967, 2016.
- 665 Joseph R Mukabana and Roger A Pielke. Investigating the influence of synoptic-scale monsoonal winds and mesoscale circulations on  
666 diurnal weather patterns over Kenya using a mesoscale numerical model. *Mon. Wea. Rev.*, 124(2):224–244, 1996.
- 667 Andrew Edwin Okeyo. The impact of Lake Victoria on the convective activities over the Kenya Highlands. *J. Meteorolog. Soc. Japan*  
668 *Ser. II*, 64:689–695, 1986.
- 669 GN Petersen and IA Renfrew. Aircraft-based observations of air–sea fluxes over Denmark Strait and the Irminger Sea during high wind  
670 speed conditions. *Quarterly Journal of the Royal Meteorological Society*, 135(645):2030–2045, 2009.

- 671 Benjamin Pohl and Pierre Camberlin. Influence of the Madden-Julian Oscillation on East African rainfall. Part I: intraseasonal variability  
672 and regional dependency. *Quart. J. Roy. Meteor. Soc.*, 132(621):2521–2539, 2006a.
- 673 Benjamin Pohl and Pierre Camberlin. Influence of the Madden-Julian Oscillation on East African rainfall. Part II: March-May season  
674 extremes and interannual variability. *Quart. J. Roy. Meteor. Soc.*, 132(621B):2541–2558, 2006b.
- 675 DD Reible, JE Simpson, and PF Linden. The sea breeze and gravity-current frontogenesis. *Quarterly Journal of the Royal Meteorolog-  
676 ical Society*, 119(509):1–16, 1993.
- 677 Gabriel Gerard Rooney and Francisco Jorge Bornemann. The performance of FLake in the Met Office Unified Model. *Tellus A*, 65(1):  
678 21363, 2013.
- 679 Irina Sandu, Anton Beljaars, Peter Bechtold, Thorsten Mauritsen, and Gianpaolo Balsamo. Why is it so difficult to represent stably  
680 stratified conditions in numerical weather prediction (NWP) models? *J. Adv. Model. Earth Syst.*, 5(2):117–133, 2013.
- 681 Johannes Schmetz, Paolo Pili, Stephen Tjemkes, Dieter Just, Jochen Kerkmann, Sergio Rota, and Alain Ratier. An introduction to  
682 Meteosat second generation (MSG). *Bull. Amer. Meteor. Soc.*, 83(7):977–992, 2002.
- 683 Carl Schreck. North Carolina Institute for Climate Studies: Tropical Monitoring. Available at: [https://ncics.org/portfolio/  
684 monitor/mjo/](https://ncics.org/portfolio/monitor/mjo/). Last accessed: 19 Aug 2019, n.d.
- 685 FHM Semazzi. Enhancing safety of navigation and efficient exploitation of natural resources over Lake Victoria and its basin by  
686 strengthening meteorological services on the lake. Technical report, North Carolina State University Climate Modeling Laboratory,  
687 2011.
- 688 JE Simpson, DA Mansfield, and JR Milford. Inland penetration of sea-breeze fronts. *Quart. J. Roy. Meteor. Soc.*, 103(435):47–76, 1977.
- 689 John E Simpson. Gravity currents in the laboratory, atmosphere, and ocean. *Annu. Rev. Fluid Mech.*, 14(1):213–234, 1982.
- 690 Yi Song, Fredrick HM Semazzi, Lian Xie, and Laban J Ogallo. A coupled regional climate model for the Lake Victoria basin of East  
691 Africa. *Int. J. Climatol.*, 24(1):57–75, 2004.
- 692 Wim Thiery, Andrey Martynov, François Darchambeau, J-P Descy, P-D Plisnier, Laxmi Sushama, and Nicole PM van Lipzig. Under-  
693 standing the performance of the FLake model over two African Great Lakes. *Geosci. Model Dev.*, 7(1):317–337, 2014.
- 694 Wim Thiery, Edouard L Davin, Hans-Jürgen Panitz, Matthias Demuzere, Stef Lhermitte, and Nicole Van Lipzig. The impact of the  
695 African Great Lakes on the regional climate. *J. Climate*, 28(10):4061–4085, 2015.
- 696 Wim Thiery, Edouard L Davin, Sonia I Seneviratne, Kristopher Bedka, Stef Lhermitte, and Nicole PM van Lipzig. Hazardous thunder-  
697 storm intensification over Lake Victoria. *Nat. Commun.*, 7:12786, 2016.
- 698 Wim Thiery, Lukas Gudmundsson, Kristopher Bedka, Fredrick HM Semazzi, Stef Lhermitte, Patrick Willems, Nicole PM van Lipzig,  
699 and Sonia I Seneviratne. Early warnings of hazardous thunderstorms over Lake Victoria. *Environ. Res. Lett.*, 12(7):074012, 2017.
- 700 Jonas Van de Walle, Wim Thiery, Oscar Brousse, Niels Souverijns, Matthias Demuzere, and Nicole PM van Lipzig. A convection-  
701 permitting model for the Lake Victoria Basin: evaluation and insight into the mesoscale versus synoptic atmospheric dynamics.  
702 *Climate Dynamics*, 54(3):1779–1799, 2020.
- 703 AK Vance, SJ Abel, RJ Cotton, and AM Woolley. Performance of WVSS-II hygrometers on the FAAM research aircraft. *Atmos. Meas.  
704 Tech.*, 8(3):1617–1625, 2015.
- 705 Pascal F Waniha, Rita D Roberts, James W Wilson, Agnes Kijazi, and Benedicto Katole. Dual-polarization radar observations of deep  
706 convection over Lake Victoria basin in East Africa. *Atmosphere*, 10(11):706, 2019.
- 707 Nigel Wood, Andrew Staniforth, Andy White, Thomas Allen, Michail Diamantakis, Markus Gross, Thomas Melvin, Chris Smith,  
708 Simon Vosper, Mohamed Zerroukat, et al. An inherently mass-conserving semi-implicit semi-Lagrangian discretization of the  
709 deep-atmosphere global non-hydrostatic equations. *Quart. J. Roy. Meteor. Soc.*, 140(682):1505–1520, 2014.

- 710 Beth J Woodhams, Cathryn E Birch, John H Marsham, Caroline L Bain, Nigel M Roberts, and Douglas FA Boyd. What Is the Added  
711 Value of a Convection-Permitting Model for Forecasting Extreme Rainfall over Tropical East Africa? *Mon. Wea. Rev.*, 146(9):  
712 2757–2780, 2018.
- 713 Beth J Woodhams, Cathryn E Birch, John H Marsham, Todd P Lane, Caroline L Bain, and Stuart Webster. Identifying key controls on  
714 storm formation over the Lake Victoria Basin. *Mon. Wea. Rev.*, 147(9):3365–3390, 2019.
- 715 Wenchang Yang, Richard Seager, Mark A Cane, and Bradfield Lyon. The Annual Cycle of East African Precipitation. *J. Climate*, 28  
716 (6):2385–2404, 2015.
- 717 Xungang Yin and Sharon E Nicholson. The water balance of Lake Victoria. *Hydrol. Sci. J.*, 43(5):789–811, 1998.
- 718 M Zerroukat and BJ Shipway. ZLF (Zero Lateral Flux): A simple mass conservation method for semi-Lagrangian based limited area  
719 models. *Quart. J. Roy. Meteor. Soc.*, 2017.